

# UAV Formation and Resource Allocation Optimization for Communication-Assisted 3D InSAR Sensing

Mohamed-Amine Lahmeri\*, Víctor Mustieles-Pérez\*<sup>†</sup>, Martin Vossiek\*, Gerhard Krieger\*<sup>†</sup>,  
and Robert Schober\*

\*Friedrich-Alexander-Universität Erlangen-Nürnberg (FAU), Germany

<sup>†</sup>German Aerospace Center (DLR), Microwaves and Radar Institute, Weßling, Germany

## Abstract

In this paper, we investigate joint unmanned aerial vehicle (UAV) formation and resource allocation optimization for communication-assisted three-dimensional (3D) synthetic aperture radar (SAR) sensing. We consider a system consisting of two UAVs that perform bistatic interferometric SAR (InSAR) sensing for generation of a digital elevation model (DEM) and transmit the radar raw data to a ground station (GS) in real time. To account for practical 3D sensing requirements, we use non-conventional sensing performance metrics, such as the interferometric coherence, i.e., the local cross-correlation between the two co-registered UAV SAR images, the point-to-point InSAR relative height error, and the height of ambiguity, which together characterize the accuracy with which the InSAR system can determine the height of ground targets. Our objective is to jointly optimize the UAV formation, speed, and communication power allocation for maximization of the InSAR coverage while satisfying energy, communication, and InSAR-specific sensing constraints. To solve the formulated non-smooth and non-convex optimization problem, we divide it into three sub-problems and propose a novel alternating optimization (AO) framework that is based on classical, monotonic, and stochastic optimization techniques. The effectiveness of the proposed algorithm is validated through extensive simulations and compared to several benchmark schemes. Furthermore, our simulation results highlight the impact of the UAV-GS communication link on the flying formation and sensing performance and show that the DEM of a large area of interest can be mapped and offloaded to ground successfully, while the ground topography can be estimated with centimeter-scale precision. Lastly, we demonstrate that a low UAV velocity is preferable for InSAR applications as it leads to better sensing accuracy.

This paper is presented in part at the IEEE International Conference on Communication, Denver, USA, Jun. 2024 [1]. This work was supported in part by the Deutsche Forschungsgemeinschaft (DFG, German Research Foundation) GRK 2680 – Project-ID 437847244.

## I. INTRODUCTION

The widespread use of unmanned aerial vehicles (UAVs) has revolutionized modern technology, impacting fields like remote sensing, communication, and disaster monitoring [2]. Specifically, UAVs excel in remote sensing applications using a variety of technologies, such as cameras, lidars, and radars. Among these technologies, radar sensing has attracted particular attention due to its capacity to operate day and night under all weather conditions. Radar sensing applications can be classified into three distinct categories based on the dimensionality of the extracted information. Firstly, one-dimensional (1D) sensing includes applications such as ranging and detection and necessitates at least one radar antenna. Secondly, two-dimensional (2D) sensing, also known as radar imaging, can be realized using, e.g., multiple-input multiple-output (MIMO) radar systems employing multiple antennas [3] or by moving a single radar antenna or a MIMO array along a trajectory to create a synthetic aperture radar (SAR) or MIMO-SAR system, and can provide a high-resolution image of the illuminated area [4]. Lastly, three-dimensional (3D) sensing provides an additional dimension besides the 2D spatial location of a target, such as its altitude above ground. Here, an interesting remote sensing technique that can be used to generate accurate 3D digital elevation models (DEMs) is across-track interferometric SAR (InSAR) [4]. In the following subsection, we discuss 1D and 2D UAV-based sensing applications, focusing on the existing trajectory and resource optimization frameworks. Then, in Subsection I-B, we address UAV-based 3D sensing applications, focusing on InSAR applications, which are the main topic of interest in this paper.

### A. Existing Optimization Frameworks for UAV-based 1D and 2D Sensing

For 1D sensing, the joint optimization of the trajectory and beamforming of UAV-based integrated sensing and communication systems has been studied to minimize the average power consumption [5] and to maximize the achievable communication rate for both single-user [6] and multi-user [7] scenarios. For 2D sensing, trajectory optimization for UAV-based SAR was investigated in [8]–[15]. In [9]–[11], the backscattered signal was received by a UAV, while the target area was illuminated by a geosynchronous satellite. In [8], [12], [14], [15], UAVs were used as transmitters and receivers and, in [13], a UAV was used as receiver, while the target area was illuminated by a communication base station. For these systems, seamless UAV-to-ground connectivity enables the timely transfer of essential information to the ground for processing. In fact, the authors in [11], [14], [15] assumed a line-of-sight (LOS) link between the UAV-SAR system and a ground station (GS), and, in [14], [15], real-time offloading to the GS was considered, while in [11], the authors investigated transmitting the total radar raw data to the ground. In general, trajectory and resource allocation optimization for UAV-based sensing has been extensively studied in the

literature. However, most works focus on 1D or 2D sensing applications. Although a performance analysis for 3D sensing applications was provided in [16]–[18], the joint UAV formation and resource allocation optimization for such applications has not been studied yet.

### *B. UAV-based 3D Sensing via InSAR*

Across-track InSAR is an interesting 3D remote sensing technique that requires the use of more than one radar antenna. At least two radar antennas are moved to illuminate a given target area from different angles, such that at least two SAR images can be formed. All possible image pairs are first co-registered [19], i.e., aligned such that each ground point corresponds to the same pixel in both images, and based on the phase difference, an interferogram is created to extract information about the topography of the target area [19], [20]. InSAR-based 3D sensing is fundamentally different from 1D and 2D sensing. In particular, to assess the performance of 1D sensing, conventional metrics, such as signal-to-noise ratio (SNR) [5], beam pattern gain [6], [7], and probability of detection and false alarm [21], [22] can be adopted. For 2D sensing, image performance metrics can be used, including SAR SNR [14], spatial resolution [9], and integrated sidelobe ratio (ISLR) and peak sidelobe ratio (PSLR) [23]. However, these performance metrics are not sufficient for 3D sensing applications, such as generating an accurate DEM based on across-track interferometry. In fact, the key performance metric for estimating interferometric performance is coherence, which is a function of the correlation between the pair of co-registered SAR images [20]. Additional relevant performance metrics are the height of ambiguity (HoA), which is a proportionality constant between the interferometric phase and the terrain height and is thus related to the sensitivity of the radar to the ground topography [20], and the relative height accuracy, which represents the accuracy with which the altitude of ground objects (i.e., the ground topography) can be estimated. In this context, an interesting trade-off arises; while a large inter-UAV separation distance, i.e., a large interferometric baseline, leads to a small HoA, which in general improves the height accuracy of DEMs, it also leads to a degradation of the image coherence [18]. Furthermore, 3D InSAR sensing is different from cooperative sensing [21], [24] for two main reasons. In particular, for 3D InSAR (i) the coverage is defined by the region where the ground footprints of the two radar antennas overlap and (ii) the sensing performance is highly dependent on the UAV formation. Moreover, compared to 1D and 2D sensing, 3D sensing is more challenging due to the use of multiple sensors and the need for considering the aforementioned dedicated performance metrics. Specifically, relying solely on beam pattern design, SNR, or resolution is not sufficient for 3D applications. Therefore, based on the above discussion, existing results for UAV-based 1D and 2D sensing are not applicable to interferometric 3D sensing.

### C. Main Contributions

In this paper, we consider a system of two UAVs that perform SAR sensing of a given area from different angles, such that the difference of the sensors' phases allows for estimating the height of ground objects based on InSAR techniques. For this system, we maximize the sensing coverage by jointly optimizing the formation, velocity, and communication transmit power of both UAVs while satisfying practical energy, communication, and sensing constraints. Our main contributions can be summarized as follows:

- Different from existing works targeting 1D and 2D sensing applications, we consider InSAR-specific sensing performance metrics, such as InSAR coverage, coherence, HoA, and relative height accuracy, that can capture the quality of DEMs.
- A joint UAV formation and resource allocation optimization problem is formulated to maximize the sensing coverage while satisfying practical energy, communication, and sensing constraints.
- A novel alternating optimization (AO)-based algorithm, which incorporates classical, monotonic, and stochastic optimization techniques, is proposed to solve the formulated challenging non-smooth and non-convex optimization problem.
- Our simulations show the superior performance of the proposed solution compared to a conventional AO algorithm and other benchmark schemes and unveil the impact of the InSAR-specific sensing requirements on communication and vice versa.

We note that this article extends a corresponding conference version [1]. In contrast to this paper, in [1], the velocity of both the master and slave UAVs was fixed and the radar look angle of the slave drone was also not optimized. Furthermore, the minimum sensing data rate was assumed to be fixed, i.e., independent of the imageable area. Lastly, the relative point-to-point height accuracy was not accounted for in [1].

The remainder of this paper is organized as follows. In Section II, we present the considered system. In Section III, the formation and resource allocation problem is formulated, and the proposed solution is presented in Section IV. In Section V, the performance of the proposed scheme is assessed via simulations, and finally, conclusions are drawn in Section VI.

*Notations:* In this paper, lower-case letters  $x$  refer to scalar variables, while boldface lower-case letters  $\mathbf{x}$  denote vectors.  $\{a, \dots, b\}$  denotes the set of all integers between  $a$  and  $b$  and  $\emptyset$  denotes an empty set.  $|\cdot|$  denotes the absolute value operator.  $\mathbb{R}^N$  represents the set of all  $N$ -dimensional vectors with real-valued entries. For a vector  $\mathbf{x} = (x_1, \dots, x_N)^T \in \mathbb{R}^N$ ,  $\|\mathbf{x}\|_2$  denotes the Euclidean norm, whereas  $\mathbf{x}^T$  stands for the transpose of  $\mathbf{x}$ . For real-valued multivariate functions  $f(\mathbf{x})$  and  $g(\mathbf{x})$ ,  $\frac{\partial f}{\partial \mathbf{x}}(\mathbf{a}) = \left( \frac{\partial f}{\partial x_1}(\mathbf{a}), \dots, \frac{\partial f}{\partial x_N}(\mathbf{a}) \right)^T$  denotes the partial derivative of  $f$  with respect to (w.r.t.)  $\mathbf{x}$  evaluated for an arbitrary vector  $\mathbf{a}$  and  $f(x) \otimes g(x)$  refers to the convolution operation. For real numbers  $a$  and  $b$ ,  $\max(a, b)$  and  $\min(a, b)$  stand for the maximum and

TABLE I: List of variables.

Variable	Definition
$\mathbf{p}_t[n]$	Coordinates of the reference ground target
$\mathbf{v}$	UAV velocity vector in 3D space
$v_y[n]$	UAV velocity along $y$ -axis in time slot $n$
$\mathbf{q}_i[n]$	3D position of UAV $U_i, i \in \{1, 2\}$ , in time slot $n$
$\mathbf{q}_i$	2D position of UAV $U_i, i \in \{1, 2\}$ , in $xz$ -plane
$b$ and $b_\perp$	Interferometric baseline and its perpendicular component
$\theta_2$	Radar look angle of slave UAV $U_2$
$\alpha$	Angle between the baseline and the horizontal plane
$r_i$	Radar slant range of UAV $U_i, i \in \{1, 2\}$ , w.r.t. $\mathbf{p}_t$
$S$	Common radar swath width between $U_1$ and $U_2$
$C_N$	Total InSAR coverage
$\text{SNR}_{i,n}$	SNR achieved by UAV $U_i, i \in \{1, 2\}$ , in time slot $n$
$\gamma_{\text{SNR},n}$	SNR decorrelation in time slot $n$
$\gamma_{\text{Rg}}$	Baseline decorrelation
$\gamma_n$	Total InSAR coherence in time slot $n$
$h_{\text{amb}}$	Height of ambiguity
$\Delta\phi_{90\%}$	90% percentile of the random phase error
$\Delta h_{90\%}$	Point-to-point relative height error
$P_{\text{com},i}[n]$	Instantaneous communication power consumed by $U_i$
$d_{i,n}$	Distance $U_i, i \in \{1, 2\}$ , to GS in time slot $n$
$R_{i,n}$	Instantaneous throughput from $U_i, i \in \{1, 2\}$ , to GS
$R_{\text{min},i}$	SAR sensing data rate achieved by $U_i, i \in \{1, 2\}$ .
$P_{\text{prop},n}$	UAV propulsion power in time slot $n$
$E_{i,N}$	Total energy consumed by $U_i, i \in \{1, 2\}$ , in time slot $n$

minimum of  $a$  and  $b$ , respectively. For a scalar  $x \in \mathbb{R}$ ,  $[x]^+$  refers to  $\max(0, x)$ . The notation  $X_n(\mathbf{x}_1, \dots, \mathbf{x}_i)$  highlights that  $X$  depends on optimization variables  $(\mathbf{x}_1, \dots, \mathbf{x}_i)$  and time slot  $n$ . In Table I, we present the most important variables used in the paper.

## II. SYSTEM MODEL

We consider two rotary-wing<sup>1</sup> UAVs, denoted by  $U_1$  and  $U_2$ , that perform InSAR sensing over a given area of interest. The two UAV-SAR systems move along separate linear trajectories above the target area, and each UAV captures a different SAR image of the same ground area. The two SAR images obtained

<sup>1</sup>The results presented in this paper can be extended to fixed-wing UAVs by considering a corresponding propulsion power model.

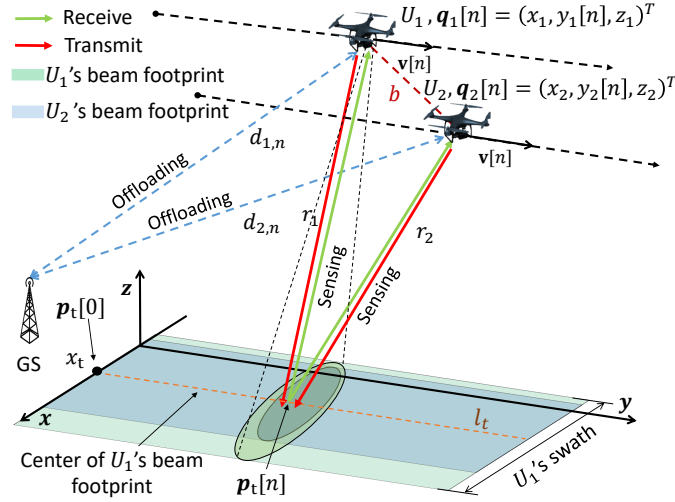


Fig. 1: InSAR sensing system with two UAV SAR sensors and a GS for real-time data offloading.

are then combined using interferometry techniques, where the phase difference between both images is exploited to generate an accurate 3D DEM. We adopt a 3D coordinate system, where the  $x$ -axis represents the ground range direction, the  $y$ -axis represents the azimuth direction, and the  $z$ -axis defines the flying altitude of the drones above ground, see Figure 1. We discretize the total mission time  $T$  into  $N$  uniform time slots of duration  $\delta_t$  such that  $T = N \cdot \delta_t$ . Both drones follow a linear trajectory as the stripmap SAR imaging mode, typically used in InSAR systems, is employed [25]. Therefore, the radar coverage along the  $x$ -axis, referred to as swath, is centered w.r.t. a line  $l_t$  that is parallel to the  $y$ -axis and passes, in time slot  $n \in \{1, \dots, N\}$ , through reference point  $\mathbf{p}_t[n] = (x_t, y[n], 0)^T \in \mathbb{R}^3$ , see Figure 1. Without loss of generality,  $U_1$  is the farthest UAV from  $\mathbf{p}_t[n]$ ,  $\forall n$ , and is referred to as the master drone, whereas  $U_2$  is the slave drone. Moreover, we consider across-track interferometry [19], where both drones transmit and receive echoes and are located in the same  $xz$ -plane, also referred to as the across-track plane [19]. They fly with the same velocity  $\mathbf{v}_y = (v_y[1], \dots, v_y[N])^T \in \mathbb{R}^N$ , such that in time slot  $n$ , the instantaneous velocity vector is given by  $\mathbf{v}[n] = (0, v_y[n], 0)^T \in \mathbb{R}^3, \forall n$ , [17]. The location of  $U_i$  in time slot  $n$ ,  $i \in \{1, 2\}$ , is denoted by  $\mathbf{q}_i[n] = (x_i, y[n], z_i)^T$ , where the  $y$ -axis position vector  $\mathbf{y} = (y[1] = 0, y[2], \dots, y[N])^T \in \mathbb{R}^N$  is given by:

$$y[n+1] = y[n] + v_y[n]\delta_t, \forall n \in \{1, N-1\}. \quad (1)$$

Hereinafter, for ease of notation, we use  $\mathbf{q}_i = (x_i, z_i)^T \in \mathbb{R}^2, \forall i \in \{1, 2\}$ , to denote the position of  $U_i$  in the across-track plane (i.e.,  $xz$ -plane), see Figure 2, whereas  $\mathbf{q}_i[n]$  refers to the full 3D position of UAV  $U_i$  in time slot  $n$ . Furthermore, the interferometric baseline, which refers to the distance between the two

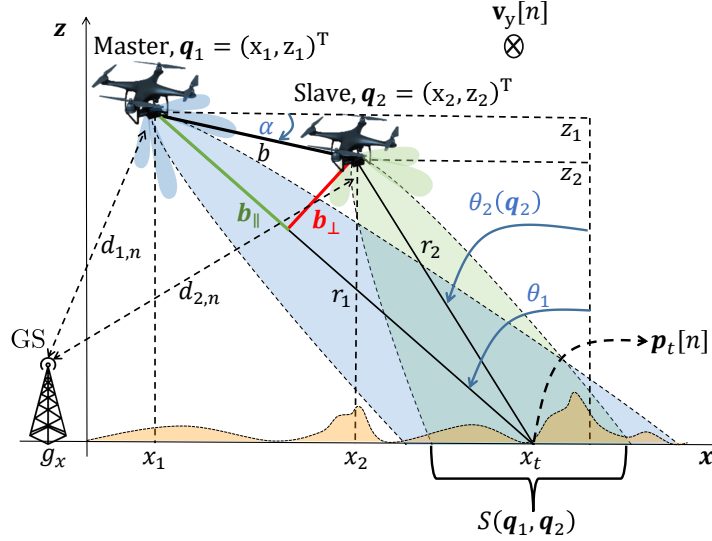


Fig. 2: Illustration of the bistatic UAV formation, denoted by  $\{\mathbf{q}_1, \mathbf{q}_2\}$ , in the across-track plane (i.e.,  $xz$ -plane).

InSAR sensors, is given by:

$$b(\mathbf{q}_1, \mathbf{q}_2) = \|\mathbf{q}_2 - \mathbf{q}_1\|_2. \quad (2)$$

The perpendicular baseline, denoted by  $b_\perp$ , is the magnitude of the projection of the baseline vector perpendicular to  $U_1$ 's LOS to  $\mathbf{p}_t[n]$  and is given by:

$$b_\perp(\mathbf{q}_1, \mathbf{q}_2) = b(\mathbf{q}_1, \mathbf{q}_2) \cos(\theta_1 - \alpha(\mathbf{q}_1, \mathbf{q}_2)), \quad (3)$$

where  $\theta_1$  is the fixed angle that  $U_1$ 's LOS to  $\mathbf{p}_t[n]$  has with the vertical, i.e., the look angle of the master UAV, and  $\alpha(\mathbf{q}_1, \mathbf{q}_2)$  is the angle between the interferometric baseline and the horizontal plane, see Figure 2.

### A. Bistatic InSAR Coverage

Let  $r_1$  and  $r_2$  denote the slant range of the radars of  $U_1$  and  $U_2$  w.r.t.  $\mathbf{p}_t[n]$ , respectively. These slant ranges are independent of time and given by:

$$r_i(\mathbf{q}_i) = \sqrt{(x_i - x_t)^2 + z_i^2}, \forall i \in \{1, 2\}. \quad (4)$$

To maximize the coverage, the master UAV is positioned in the across-track plane such that its SAR antenna beam footprint on the ground is centered around  $\mathbf{p}_t[n]$ . Furthermore, without loss of generality, we assume  $r_2(\mathbf{q}_2) \leq r_1(\mathbf{q}_1)$  and impose the following condition:

$$x_1 = x_t - z_1 \tan(\theta_1). \quad (5)$$

As the look angle of the master platform is fixed to  $\theta_1$ , we propose to adjust the look angle of the slave UAV, denoted by  $\theta_2(\mathbf{q}_2)$ , such that its beam footprint is centered around  $\mathbf{p}_t[n]$ , i.e.,  $\theta_2(\mathbf{q}_2) = \arctan\left(\frac{x_2 - x_t}{z_2}\right)$ . The InSAR coverage is limited to the area where the beam footprints of  $U_1$  and  $U_2$  overlap, see Figure 2. In this work, we focus on a single scan (i.e., single swath) for the two drones, where the usable swath can be obtained as follows:

$$S(\mathbf{q}_1, \mathbf{q}_2) = \left[ \min(S_{\text{far}}(\mathbf{q}_1), S_{\text{far}}(\mathbf{q}_2)) - \max(S_{\text{near}}(\mathbf{q}_1), S_{\text{near}}(\mathbf{q}_2)) \right]^+, \quad (6)$$

where  $S_{\text{far}}(\mathbf{q}_i) = x_i + z_i \tan(\theta_i(\mathbf{q}_i) + \frac{\Theta_{3\text{dB}}}{2})$ ,  $S_{\text{near}}(\mathbf{q}_i) = x_i + z_i \tan(\theta_i(\mathbf{q}_i) - \frac{\Theta_{3\text{dB}}}{2})$ ,  $\forall i \in \{1, 2\}$ ,  $\theta_1(\mathbf{q}_1) = \theta_1$ , and  $\Theta_{3\text{dB}}$  is the -3 dB beamwidth in elevation. The total area covered by the InSAR radar is approximated<sup>2</sup> as follows:

$$C_N(\mathbf{q}_1, \mathbf{q}_2, \mathbf{v}_y) = \sum_{n=1}^{N-1} S(\mathbf{q}_1, \mathbf{q}_2) v_y[n] \delta_t. \quad (7)$$

### B. InSAR Performance Metrics

In practical InSAR missions, such as TanDEM-X and SRTM [20], the performance requirements for DEMs are typically defined in terms of coverage and height accuracy. The height accuracy, i.e., the precision with which the ground topography can be estimated, depends on several intermediate performance metrics, specifically the coherence and the HoA. In the following, we introduce these key 3D sensing performance metrics and highlight their impact on the overall InSAR performance.

1) *Total InSAR Coherence*: The interferometric coherence, denoted by  $\gamma_n \in [0, 1]$ , represents the cross-correlation between the master and slave SAR images. In general, coherence values close to 1 result in improved sensing accuracy [20]. The total coherence can be decomposed into several decorrelation sources as follows:

$$\gamma_n = \gamma_{\text{Rg}} \gamma_{\text{SNR},n} \gamma_{\text{other}}, \forall n, \quad (8)$$

where  $\gamma_{\text{Rg}} \in [0, 1]$  denotes the baseline decorrelation,  $\gamma_{\text{SNR},n} \in [0, 1]$  is the SNR decorrelation, and  $\gamma_{\text{other}} \in [0, 1]$  represents the contribution from all other decorrelation sources, e.g., volumetric decorrelation. Here, we assume that surface scattering is dominant and  $\gamma_{\text{other}}$  is independent of the formation. [20], and that no prior knowledge about the imaged scene is available.

2) *SNR Decorrelation*: Low SNRs in SAR data acquisition result in a loss of the coherence between the master and slave SAR images during processing, causing a degradation of the sensing accuracy. In time slot  $n$ , the corresponding SNR decorrelation is given by [17]:

$$\gamma_{\text{SNR},n}(\mathbf{q}_1, \mathbf{q}_2, \mathbf{v}_y) = \prod_{i \in \{1,2\}} \frac{1}{\sqrt{1 + \text{SNR}_{i,n}^{-1}(\mathbf{q}_i, \mathbf{v}_y)}}, \forall n, \quad (9)$$

<sup>2</sup>The approximation is due to the elliptical shape of the beam footprint on the ground and becomes negligible for large  $N$ .

where  $\text{SNR}_{i,n}$  denotes the SNR achieved by  $U_i$  in time slot  $n$  and is given by [17]:

$$\text{SNR}_{i,n}(\mathbf{q}_i, \mathbf{v}_y) = \frac{\gamma_{r,i}}{v_y[n]r_i^3(\mathbf{q}_i) \sin(\theta_i(\mathbf{q}_i))}, \forall n, \quad (10)$$

where  $\gamma_{r,i} = \frac{\sigma_0 P_{t,i} G_t G_r \lambda^3 c \tau_p \text{PRF}}{4^4 \pi^3 k_b T_{\text{sys}} B_{\text{Rg}} F L_{\text{atm}} L_{\text{sys}} L_{\text{az}}}$ ,  $\forall i \in \{1, 2\}$ . Here,  $\sigma_0$  is the normalized backscatter coefficient,  $P_{t,i}$  is  $U_i$ 's radar transmit power,  $G_t$  and  $G_r$  are the transmit and receive antenna gains, respectively,  $\lambda$  is the wavelength,  $c$  is the speed of light,  $\tau_p$  is the pulse duration, PRF is the pulse repetition frequency,  $k_b$  is the Boltzmann constant,  $T_{\text{sys}}$  is the receiver noise temperature,  $B_{\text{Rg}}$  is the bandwidth of the radar pulse,  $F$  is the noise figure, and  $L_{\text{atm}}$ ,  $L_{\text{sys}}$ , and  $L_{\text{az}}$  represent the atmospheric, system, and azimuth losses, respectively. Note that, in (9), low master and slave SNRs lead to small  $\gamma_{\text{SNR},n}$ , and thus, degraded coherence  $\gamma_n$ .

3) *Baseline Decorrelation*: The baseline decorrelation  $\gamma_{\text{Rg}}$  reflects the loss of coherence caused by the different incidence angles used for acquisition of the two SAR images. The baseline decorrelation is given by [26]:

$$\gamma_{\text{Rg}}(\mathbf{q}_2) = \frac{(2 + B_p) \sin(\theta_2(\mathbf{q}_2)) - (2 - B_p) \sin(\theta_1)}{B_p (\sin(\theta_1) + \sin(\theta_2(\mathbf{q}_2)))}, \quad (11)$$

where  $B_p = \frac{B_{\text{Rg}}}{f_0}$  is the fractional bandwidth and  $f_0$  is the radar center frequency. It can be shown that UAV formations with large inter-UAV distance, which corresponds to large perpendicular baselines  $b_{\perp}$ , cause high baseline decorrelation (i.e.,  $\gamma_{\text{Rg}} \rightarrow 0$ ) and, therefore, degrade the overall coherence.

4) *Height of Ambiguity (HoA)*: The HoA is defined as the height difference that results in a complete  $2\pi$  cycle of the interferometric phase [17]. It is therefore related to the sensitivity of the radar system to topographic height variations. Similar to the baseline decorrelation, the HoA depends on the UAV formation and is given by [17]:

$$h_{\text{amb}}(\mathbf{q}_1, \mathbf{q}_2) = \frac{\lambda r_1(\mathbf{q}_1) \sin(\theta_1)}{b_{\perp}(\mathbf{q}_1, \mathbf{q}_2)}. \quad (12)$$

Note that large perpendicular baselines  $b_{\perp}$  lead to small HoA values, which result in increased errors for interferometric phase unwrapping [27]. However, very small UAV baselines, i.e., large HoAs, are not a good choice either, since they lead to low sensing accuracy, as we explain in the following.

5) *Sensing Height Accuracy*: A common statistics-based performance metric for assessing the accuracy of the height estimation in DEM is the point-to-point 90% relative height error given by [17]:

$$\Delta h_{90\%}(\mathbf{q}_1, \mathbf{q}_2, \gamma_n) = h_{\text{amb}}(\mathbf{q}_1, \mathbf{q}_2) \frac{\Delta \phi_{90\%}(\gamma_n)}{2\pi}, \quad (13)$$

where  $\Delta \phi_{90\%}$  is defined as the 90% percentile of the random phase error  $\Delta \phi$  and obtained by evaluating the difference between two random variables, each of them describing the fluctuation of the interferometric phase within one interferogram as follows [17]:

$$\int_{-\Delta \phi_{90\%}(\gamma_n)}^{\Delta \phi_{90\%}(\gamma_n)} p_{\Delta \phi}(\Delta \phi, \gamma_n) \otimes p_{\Delta \phi}(\Delta \phi, \gamma_n) \cdot d\Delta \phi = 0.9, \quad (14)$$

where  $p_{\Delta\phi}$  is the probability density function (PDF) of the phase error  $\Delta\phi$  for a given interferometric coherence  $\gamma$  and is given by<sup>3</sup> [28]:

$$p_{\Delta\phi}(\Delta\phi, \gamma_n) = \frac{\Gamma(n_L + 0.5)(1 - |\gamma_n|^2)^{n_L} |\gamma_n| \cos(\Delta\phi)}{2\sqrt{\pi}\Gamma(n_L) (1 - |\gamma_n|^2 \cos^2(\Delta\phi))^{n_L+0.5}} + \frac{(1 - |\gamma_n|^2)^{n_L}}{2\pi} F_G(n_L, 1; 0.5; |\gamma_n|^2 \cos^2(\Delta\phi)). \quad (15)$$

Here,  $\Gamma$  is the Gamma function,  $F_G$  is the Gauss hypergeometric function [17], and  $n_L$  is the number of independent looks. In fact, multi-looking is a technique that averages adjacent pixels of the interferogram, e.g., by filtering with a boxcar window, to improve phase estimation leading to a trade-off between spatial resolution and height accuracy, see [28]. Note that large HoAs result in large point-to-point 90% height errors  $\Delta h_{90\%}$ , and thus, in low relative height estimation accuracy. This explains why optimizing the UAV baseline, and therefore, the HoA, is an intricate problem.

### C. Communication Performance

We consider real-time offloading of the radar data to a GS, where the master and slave UAVs employ frequency-division multiple-access (FDMA). The instantaneous communication transmit power consumed by UAV  $U_i$  is given by  $\mathbf{P}_{\text{com},i} = (P_{\text{com},i}[1], \dots, P_{\text{com},i}[N])^T \in \mathbb{R}^N, i \in \{1, 2\}$ . We denote the location of the GS by  $\mathbf{g} = (g_x, g_y, g_z)^T \in \mathbb{R}^3$  and the distance from  $U_i$  to the GS by  $d_{i,n}(\mathbf{q}_i, \mathbf{v}_y) = \|\mathbf{q}_i[n] - \mathbf{g}\|_2, \forall i \in \{1, 2\}, \forall n$ . We suppose that both UAVs fly at sufficiently high altitudes to allow obstacle-free communication with the GS over a LOS link. Thus, based on the free-space path loss model and FDMA, the instantaneous throughput from  $U_i, \forall i \in \{1, 2\}$ , to the GS is given by:

$$R_{i,n}(\mathbf{q}_i, \mathbf{P}_{\text{com},i}, \mathbf{v}_y) = B_{c,i} \log_2 \left( 1 + \frac{P_{\text{com},i}[n] \beta_{c,i}}{d_{i,n}^2(\mathbf{q}_i, \mathbf{v}_y)} \right), \forall n, \quad (16)$$

where  $B_{c,i}$  is the fixed communication bandwidth allocated for  $U_i$  and  $\beta_{c,i}$  is its reference channel gain<sup>4</sup> divided by the noise variance. The minimum required data rate, usually fixed in communication systems, is significantly impacted by the formation of the two UAVs and depends on the imageable area size. Based on [30], the SAR sensing data rate for  $U_i, \forall i \in \{1, 2\}$ , is given by:

$$R_{\min,i}(\mathbf{q}_i) = n_B B_{\text{Rg}} \text{PRF} \left( \frac{z_i}{c} \left( \frac{1}{\cos(\theta_i(\mathbf{q}_i) + \frac{\Theta_{3\text{dB}}}{2})} - \frac{1}{\cos(\theta_i(\mathbf{q}_i) - \frac{\Theta_{3\text{dB}}}{2})} \right) + \tau_p \right), \quad (17)$$

where  $n_B$  is the number of bits per complex sample.

<sup>3</sup>In [28], the PDF is derived by assuming Gaussian scattering-matrix statistics. Yet, the proposed solution can be extended to other models, e.g., the K-distribution model [29].

<sup>4</sup>The reference channel gain is the channel power gain at a reference distance of 1 m.

### D. Energy Consumption

The propulsion power  $P_{\text{prop},n}$  consumed by the drone in time slot  $n$  is given by [31]:

$$P_{\text{prop},n}(\mathbf{v}_y) = P_0 \left( 1 + \frac{3v_y^2[n]}{U_{\text{tip}}^2} \right) + P_I \left( \sqrt{1 + \frac{v_y^4[n]}{4v_0^4}} - \frac{v_y^2[n]}{2v_0^2} \right)^{\frac{1}{2}} + \frac{1}{2}d_0\rho s A_e v_y^3[n], \forall n. \quad (18)$$

Here,  $P_0 = \frac{\delta_u}{8}\rho s A_e \Omega^3 R^3$  and  $P_I = (1 + k_u) \frac{W_u^{\frac{3}{2}}}{\sqrt{2\rho A_e}}$  are two constants,  $v_0 = \sqrt{\frac{W_u}{2\rho A_e}}$  is the mean rotor induced velocity while hovering,  $U_{\text{tip}}$  is the tip speed of the rotor blade,  $d_0$  is the fuselage drag ratio,  $\delta_u$  is the profile drag coefficient,  $\rho$  is the air density,  $s$  is the rotor solidity,  $A_e$  is the rotor disc area,  $\Omega$  is the blade angular velocity,  $R$  is the rotor radius,  $k_u$  is a correction factor, and  $W_u$  is the aircraft weight in Newton. The total energy consumed by UAV  $U_i, \forall i \in \{1, 2\}$ , is given by:

$$E_{i,N}(\mathbf{P}_{\text{com},i}, \mathbf{v}_y) = \sum_{n=1}^N \delta_t \left( P_{\text{prop},n}(\mathbf{v}_y) + P_{t,i} + P_{\text{com},i}[n] \right). \quad (19)$$

## III. PROBLEM FORMULATION

In this paper, we aim to maximize the InSAR coverage by jointly optimizing the UAV formation  $\{\mathbf{q}_1, \mathbf{q}_2\}$ , the instantaneous communication transmit powers  $\{\mathbf{P}_{\text{com},1}, \mathbf{P}_{\text{com},2}\}$ , and the instantaneous UAV velocity  $\mathbf{v}_y$ , while satisfying energy, communication, and interferometric quality-of-service constraints. To this end, we formulate the following optimization problem:

$$\begin{aligned} \text{(P.1)} : \quad & \max_{\mathbf{q}_1, \mathbf{q}_2, \mathbf{P}_{\text{com},1}, \mathbf{P}_{\text{com},2}, \mathbf{v}_y} C_N(\mathbf{q}_1, \mathbf{q}_2, \mathbf{v}_y) \\ \text{s.t.} \quad & \text{C1} : z_{\min} \leq z_i \leq z_{\max}, \forall i \in \{1, 2\}, \\ & \text{C2} : x_1 = x_t - z_1 \tan(\theta_1), \\ & \text{C3} : r_2(\mathbf{q}_2) \leq r_1(\mathbf{q}_1), \\ & \text{C4} : x_2 \leq x_t, \\ & \text{C5} : b(\mathbf{q}_1, \mathbf{q}_2) \geq b_{\min}, \\ & \text{C6} : \gamma_{\text{SNR},n}(\mathbf{q}_1, \mathbf{q}_2, \mathbf{v}_y) \geq \gamma_{\text{SNR}}^{\min}, \forall n, \\ & \text{C7} : \gamma_{\text{Rg}}(\mathbf{q}_2) \geq \gamma_{\text{Rg}}^{\min}, \\ & \text{C8} : h_{\text{amb}}(\mathbf{q}_1, \mathbf{q}_2) \geq h_{\text{amb}}^{\min}, \\ & \text{C9} : \Delta h_{90\%}^{\text{worst}}(\mathbf{q}_1, \mathbf{q}_2) \leq \Delta h^{\max}, \\ & \text{C10} : 0 \leq P_{\text{com},i}[n] \leq P_{\text{com}}^{\max}, \forall i \in \{1, 2\}, \forall n, \\ & \text{C11} : R_{i,n}(\mathbf{q}_i, \mathbf{P}_{\text{com},i}, \mathbf{v}_y) \geq R_{\min,i}(\mathbf{q}_i), \forall i \in \{1, 2\}, \forall n, \end{aligned}$$

$$\text{C12} : E_{i,N}(\mathbf{P}_{\text{com},i}, \mathbf{v}_y) \leq E_{\text{max},i}, \forall i \in \{1, 2\},$$

$$\text{C13} : v_{\text{min}} \leq v_y[n] \leq v_{\text{max}}, \forall n,$$

$$\text{C14} : \theta_{\text{min}} \leq \theta_2(\mathbf{q}_2) \leq \theta_{\text{max}},$$

$$\text{C15} : \theta_2(\mathbf{q}_2) = \arctan\left(\frac{x_2 - x_t}{z_2}\right).$$

Constraint C1 specifies the maximum and minimum allowed flying altitude, denoted by  $z_{\text{max}}$  and  $z_{\text{min}}$ , respectively. Constraints C2 and C3 ensure maximum overlap between the beam footprint of the master drone and the area of interest. Constraint C4 is imposed because a side-looking SAR is assumed. Constraint C5 ensures a minimum separation distance between the UAVs, denoted by  $b_{\text{min}}$ . Constraints C6 and C7 ensure minimum required thresholds for the sensing SNR and baseline decorrelation, denoted by  $\gamma_{\text{SNR}}^{\text{min}}$  and  $\gamma_{\text{Rg}}^{\text{min}}$ , respectively. Constraint C8 imposes a minimum HoA, denoted by  $h_{\text{amb}}^{\text{min}}$ , that satisfies phase unwrapping requirements [20]. Constraint C9 ensures that the worst-case point-to-point 90% relative height error of UAV formation  $\{\mathbf{q}_1, \mathbf{q}_2\}$ , defined as  $\Delta h_{90\%}^{\text{worst}}(\mathbf{q}_1, \mathbf{q}_2) = \Delta h_{90\%}(\mathbf{q}_1, \mathbf{q}_2, \gamma_{\text{SNR}}^{\text{min}}, \gamma_{\text{Rg}}^{\text{min}}, \gamma_{\text{other}})$ , does not exceed the maximum allowed height error, denoted by  $\Delta h^{\text{max}}$ . The definition of  $\Delta h_{90\%}^{\text{worst}}$  is based on the fact that (i) an analytical expression for (14) cannot be derived and (ii) the phase error variance decreases with the coherence [28]. Therefore, (14) is solved numerically for the worst case scenario, as  $\gamma_n \geq \gamma_{\text{SNR}}^{\text{min}} \gamma_{\text{Rg}}^{\text{min}} \gamma_{\text{other}}, \forall n$ . Constraint C10 ensures that the communication transmit power is non-negative and does not exceed the maximum allowed level denoted by  $P_{\text{com}}^{\text{max}}$ . Constraint C11 ensures that the achievable throughput of drone  $U_i$  does not fall below the minimum required data rate  $R_{\text{min},i}(\mathbf{q}_i), \forall i \in \{1, 2\}$ , which depends on the imageable area, thus the UAV formation. Constraint C12 limits the total energy consumed by UAV  $U_i$  to its maximum battery capacity, denoted by  $E_{\text{max},i}, \forall i \in \{1, 2\}$ . Constraint C13 specifies the minimum and maximum allowed velocities of the UAV-SAR system, denoted by  $v_{\text{min}}$  and  $v_{\text{max}}$ , respectively. Constraint C14 limits the maximum and minimum slave look angles to  $\theta_{\text{max}}$  and  $\theta_{\text{min}}$ , respectively. Constraint C15 directs the slave look angle towards  $\mathbf{p}_t[n], \forall n$ . We note that some of the constraints do not depend on time  $n$  as some variables, such as  $x_1$  and  $z_2$ , are optimized but are fixed across all time slots due to the prescribed linear InSAR trajectory imposed by the stripmap mode SAR operation [25].

Problem (P.1) is a non-smooth non-convex optimization problem for the following reasons. First, the use of a variable slave look angle as well as max and min functions causes the objective function  $C_N$  to be non-smooth and non-convex w.r.t.  $\mathbf{q}_2$ . Second, the coupling between different optimization variables and the presence of trigonometric functions in the expressions for the SNR decorrelation, baseline decorrelation, and HoA (see (9), (11), and (12)), make constraints C6, C7, C8, and C9 non-convex. Third, the use of variable minimum sensing data rates causes C11 to be neither monotonic nor convex. Fourth, constraints

C3 and C5 involve lower bounds on Euclidean distances, and thus, they are also non-convex. Lastly, the UAV propulsion power, given in (18), causes constraint C12 to be non-convex. In short, problem (P.1) involves interesting performance trade-offs, which do not allow for a trivial solution. For instance, achieving extensive coverage requires a high speed, which reduces the sensing SNRs, leading to degraded coherence and, consequently, increased estimation errors. Furthermore, choosing a close flying formation for the UAVs can improve the coverage (due to the increased overlap of the corresponding individual images), however, it also causes the baseline to be small, which leads to high HoA, and consequently, large estimation errors. In summary, it is very difficult and challenging to find a globally optimal solution to problem (P.1). To overcome this challenge, in the next section, we divide problem (P.1) into several more tractable and easier-to-solve sub-problems and tackle them in an alternating manner.

#### IV. SOLUTION OF THE OPTIMIZATION PROBLEM

To strike a balance between performance and complexity, we provide a low-complexity sub-optimal solution for the formulated problem based on AO. To this end, in each iteration  $m$  of the proposed AO algorithm, problem (P.1) is divided into three sub-problems, namely (P.1.a), (P.1.b), and (P.1.c), that are solved alternately, as illustrated in Figure 3. In problems (P.1.a) and (P.1.b), we optimize the positions  $\mathbf{q}_2$  and  $\mathbf{q}_1$  of the slave and master UAVs in the across-track plane, respectively. In sub-problem (P.1.c), we optimize the UAV resources, namely the instantaneous velocity  $\mathbf{v}_y$  (which affects the propulsion power  $\mathbf{P}_{\text{prop}}$ ) and the instantaneous communication transmit powers,  $\mathbf{P}_{\text{com},1}$  and  $\mathbf{P}_{\text{com},2}$ . Each sub-problem has different characteristics, therefore, in the following subsections, we provide the solution for each sub-problem using different optimization techniques.

##### A. Slave UAV Optimization

In this subsection, we aim to optimize the across-track position of the slave UAV,  $\mathbf{q}_2$ , for given resources  $\{\mathbf{v}_y, \mathbf{P}_{\text{com},1}, \mathbf{P}_{\text{com},2}\}$  and given master UAV position  $\mathbf{q}_1$ . Therefore, problem (P.1) reduces to sub-problem (P.1.a) given by:

$$\begin{aligned}
 & \text{(P.1.a)} : \max_{\mathbf{q}_2} C_N(\mathbf{q}_1, \mathbf{q}_2, \mathbf{v}_y) \\
 & \text{s.t. } C3 - C9, C14, C15, \\
 & C1 : z_{\min} \leq z_2 \leq z_{\max}, \\
 & C11 : R_{2,n}(\mathbf{q}_2, \mathbf{P}_{\text{com},2}, \mathbf{v}_y) \geq R_{\min,2}(\mathbf{q}_2), \forall n.
 \end{aligned}$$

Sub-problem (P.1.a) is a non-smooth non-convex optimization problem due to its objective function and constraints C5, C7 – C9, and C11. The presence of trigonometric functions in constraints C7, C8, and C9,

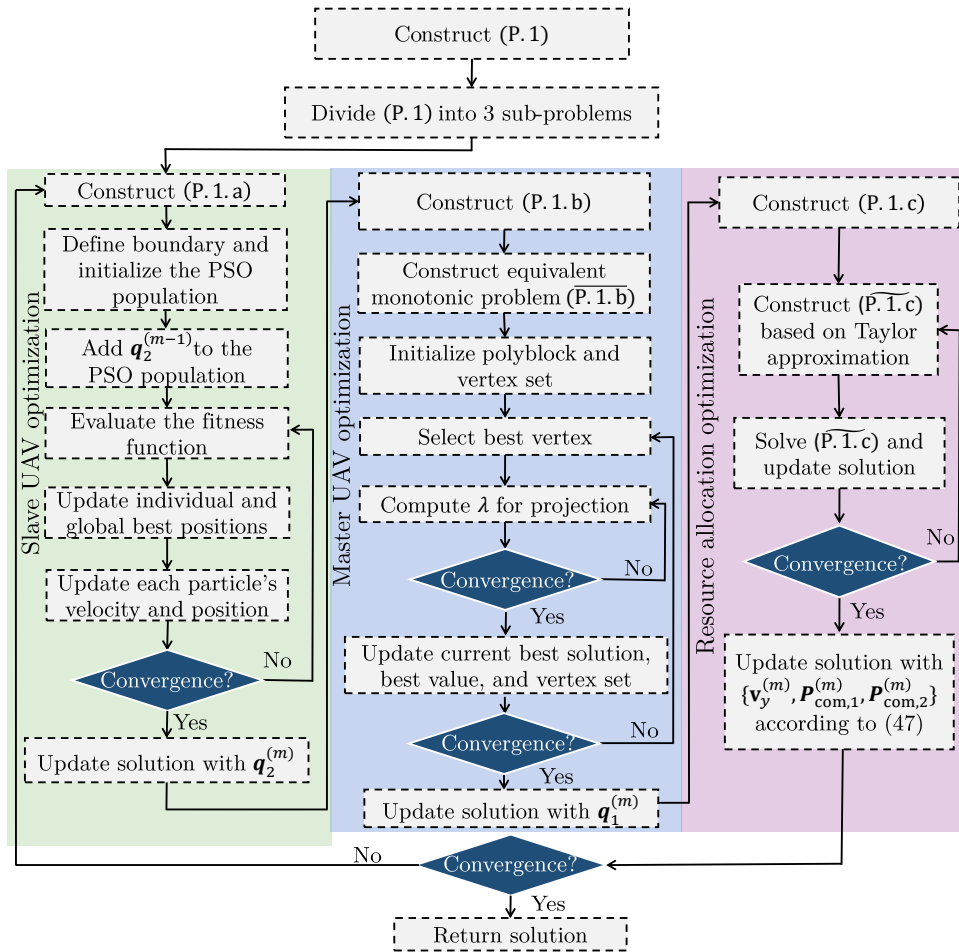


Fig. 3: Block diagram of the proposed solution to problem (P.1) based on AO, successive convex approximation (SCA), polyblock outer approximation, and particle swarm optimization (PSO).

as well as the non-smoothness of the objective function w.r.t.  $q_2$  make it very difficult to solve problem (P.1.a) using classical optimization methods that are generally based on gradient descent. Nevertheless, we provide a low-complexity close-to-optimal solution based on stochastic optimization [32]. Motivated by its success in solving complex non-smooth optimization problems and its fast convergence [33], we use particle swarm optimization (PSO), which is a population-based stochastic optimization framework that mimics the intelligent collective behavior of animals, such as birds [34]. To solve sub-problem (P.1.a), a population of  $D$  particles is employed to explore the 2D across-track plane. In iteration  $k$  of the PSO algorithm, particle  $d$ , denoted by  $\mathbf{p}_d^{(k)} \in \mathbb{R}^2, \forall d$ , has two dimensions corresponding to the  $x$ - and  $z$ -coordinates of the slave UAV as follows:

$$\mathbf{p}_d^{(k)} = (x_{2,d}^{(k)}, z_{2,d}^{(k)})^T, \forall d, \quad (20)$$

where  $x_{2,d}^{(k)}$  and  $z_{2,d}^{(k)}$  correspond to the  $x$ - and  $z$ -positions of particle  $d$  in iteration  $k$ , respectively. Furthermore, the velocity vector of particle  $d$  in iteration  $k$  is denoted by  $\mathbf{v}_{\text{PSO},d}^{(k)} \in \mathbb{R}^2$  and given by:

$$\mathbf{v}_{\text{PSO},d}^{(k)} = (v_{\text{PSO},d}^{(k)}[1], v_{\text{PSO},d}^{(k)}[2])^T, \forall d, \quad (21)$$

where  $v_{\text{PSO},d}^{(k)}[1]$  and  $v_{\text{PSO},d}^{(k)}[2]$  are the  $x$ - and  $z$ -components of the particle velocity vector, respectively. In iteration  $k \geq 2$ , the velocity of each particle is affected by its previous velocity, given by  $\mathbf{v}_{\text{PSO},d}^{(k-1)}$ , its previous local experience, given by its previous local best-known position, denoted by  $\mathbf{p}_{\text{best},d}^{(k-1)} \in \mathbb{R}^2$ , and its global experience, given by the best-known position, denoted by  $\mathbf{p}_{\text{best}}^{(k-1)} \in \mathbb{R}^2$ , as shown below [35]:

$$\mathbf{v}_{\text{PSO},d}^{(k)} = \underbrace{w(k-1)\mathbf{v}_{\text{PSO},d}^{(k-1)}}_{\text{Inertial term}} + \underbrace{c_1\mathcal{R}_1(\mathbf{p}_{\text{best},d}^{(k-1)} - \mathbf{p}_d^{(k-1)})}_{\text{Cognitive term}} + \underbrace{c_2\mathcal{R}_2(\mathbf{p}_{\text{best}}^{(k-1)} - \mathbf{p}_d^{(k-1)})}_{\text{Social term}}, \forall k \geq 2, \quad (22)$$

where  $c_1$  and  $c_2$  denote the cognitive and social learning factors, respectively,  $\mathcal{R}_1$  and  $\mathcal{R}_2$  are random variables that are uniformly distributed in  $[0, 1]$ , and  $w(k-1) \in [0, 1]$  is the inertial weight in iteration  $k-1$ . Different methods to adjust the inertial weight were proposed in the literature [36]. In this work, we employ a linearly decaying inertial weight. Moreover, the initial velocity vectors, denoted by  $\mathbf{v}_{\text{PSO},d}^{(1)}, \forall d$ , are uniformly distributed in  $[0, v_{\text{PSO}}^{\max}] \times [0, v_{\text{PSO}}^{\max}]$ , where  $v_{\text{PSO}}^{\max}$  is the maximum particle velocity. Note that the updates in (22) might cause particles to move outside of the feasible search space. To prevent this from happening and to speed up the convergence of the PSO algorithm, we define boundaries for the search space based on constraints C1 and C4 by defining a reflecting wall [37] as follows:

$$\begin{cases} v_{\text{PSO},d}^{(k)}[1] = -v_{\text{PSO},d}^{(k)}[1] & \text{if } x_{2,d}^{(k)} + v_{\text{PSO},d}^{(k)}[1] > x_t, \\ v_{\text{PSO},d}^{(k)}[2] = -v_{\text{PSO},d}^{(k)}[2] & \text{if } z_{2,d}^{(k)} + v_{\text{PSO},d}^{(k)}[2] > z_{\max} \text{ or } z_{2,d}^{(k)} + v_{\text{PSO},d}^{(k)}[2] < z_{\min}, \end{cases}, \forall d, \forall k \geq 2. \quad (23)$$

Next, in iteration  $k$ , the particle position is updated as follows:

$$\mathbf{p}_d^{(k+1)} = \mathbf{p}_d^{(k)} + \mathbf{v}_{\text{PSO},d}^{(k)}, \forall d, \forall k \geq 1, \quad (24)$$

where initial particles  $\mathbf{p}_d^{(1)}, \forall d$ , are uniformly distributed in  $[x_t - O, x_t] \times [z_{\min}, z_{\max}]$  according to C1 and C4, where  $O$  is set large enough, such that the two drones are placed sufficiently behind  $x_t$ , see constraint C4. The remaining constraints of sub-problem (P.1.a) as well as the objective function are used to construct a fitness function necessary to evaluate a given particle of the population. While the PSO algorithm was originally proposed to solve unconstrained optimization problems [34], several variations have been proposed to accommodate constraints, e.g., [35], [38], [39]. In this work, we adopt a non-parameterized PSO algorithm, which was proposed in [39]. In particular, our fitness function  $\mathcal{F}$  is given by:

$$\mathcal{F}(\mathbf{p}_d^{(k)}) = \begin{cases} C_N(\mathbf{q}_1, \mathbf{p}_d^{(k)}, \mathbf{v}_y), & \text{if } \mathbf{p}_d^{(k)} \in S, \\ \min_{k,d} \left( C_N(\mathbf{q}_1, \mathbf{p}_d^{(k)}, \mathbf{v}_y) \right) + \sum_{l \in \mathcal{L}} g_l(\mathbf{p}_d^{(k)}), & \text{if } \mathbf{p}_d^{(k)} \notin S, \end{cases} \quad \forall d, \quad (25)$$

where  $S$  is the feasible set for sub-problem (P.1.a), which is defined by constraints C3, C5 – C9, C11, C14, and C15, and functions  $g_l, l \in \mathcal{L} = \{3, 5, 6, 7, 8, 9, 11, 14\}$ , which are used as metrics to quantify constraint violations as follows:

$$g_3(\mathbf{p}_d^{(k)}) = \left[ r_2(\mathbf{p}_d^{(k)}) - r_1(\mathbf{q}_1) \right]^+, \forall d, \quad (26)$$

$$g_5(\mathbf{p}_d^{(k)}) = \left[ b_{\min} - b(\mathbf{q}_1, \mathbf{p}_d^{(k)}) \right]^+, \forall d, \quad (27)$$

$$g_6(\mathbf{p}_d^{(k)}) = \left[ \gamma_{\text{SNR}}^{\min} - \sum_{n=1}^N \gamma_{\text{SNR},n}(\mathbf{q}_1, \mathbf{p}_d^{(k)}, \mathbf{v}_y) \right]^+, \forall d, \quad (28)$$

$$g_7(\mathbf{p}_d^{(k)}) = \left[ \gamma_{\text{Rg}}^{\min} - \gamma_{\text{Rg}}(\mathbf{p}_d^{(k)}) \right]^+, \forall d, \quad (29)$$

$$g_8(\mathbf{p}_d^{(k)}) = \left[ h_{\text{amb}}^{\min} - h_{\text{amb}}(\mathbf{q}_1, \mathbf{p}_d^{(k)}) \right]^+, \forall d, \quad (30)$$

$$g_9(\mathbf{p}_d^{(k)}) = \left[ \Delta h_{90\%}^{\text{worst}}(\mathbf{q}_1, \mathbf{p}_d^{(k)}) - \Delta h^{\max} \right]^+, \forall d, \quad (31)$$

$$g_{11}(\mathbf{p}_d^{(k)}) = \left[ R_{\min,2}(\mathbf{p}_d^{(k)}) - \sum_{n=1}^N R_{2,n}(\mathbf{p}_d^{(k)}, \mathbf{P}_{\text{com},2}, \mathbf{v}_y) \right]^+, \forall d, \quad (32)$$

$$g_{14}(\mathbf{p}_d^{(k)}) = \left[ \left( \theta_{\min} - \theta_2(\mathbf{p}_d^{(k)}) \right) + \left( \theta_2(\mathbf{p}_d^{(k)}) - \theta_{\max} \right) \right]^+, \forall d. \quad (33)$$

The proposed procedure to solve sub-problem (P.1.a) is summarized in **Algorithm 1**. According to our simulations, **Algorithm 1** converges to a close-to-optimal solution, which can be assessed using an upper bound for (P.1.a);  $C_N(\mathbf{q}_1, \mathbf{q}_2, \mathbf{v}_y) \leq (S_{\text{far}}(\mathbf{q}_1) - S_{\text{near}}(\mathbf{q}_1)) \sum_{n=1}^{N-1} v_y[n] \delta_t$ . Next, we analyze the worst-case computational time complexity of **Algorithm 1**. To this end, let  $M_1$  be the maximum number of iterations for **Algorithm 1**. Then, to evaluate the fitness function for each particle,  $2N + 6$  computations are required, see (26)-(33). Therefore, the initialization of **Algorithm 1** requires  $1 + 3D + D(2N + 6)$  computations. Consequently, the overall worst-case time complexity of **Algorithm 1** is given by  $\mathcal{O}(1 + 3D + D(2N + 6) + M_1D(4 + 2N + 6))$ , which is equivalent to  $\mathcal{O}(M_1DN)$ .

### B. Master UAV Position Optimization

Next, we focus on optimizing the master UAV position in the across-track plane,  $\mathbf{q}_1$ , for given  $\{\mathbf{v}_y, \mathbf{P}_{\text{com},1}, \mathbf{P}_{\text{com},2}, \mathbf{q}_2\}$ . In this case, problem (P.1) reduces to sub-problem (P.1.b) given by:

$$(P.1.b) : \max_{\mathbf{q}_1} C_N(\mathbf{q}_1, \mathbf{q}_2, \mathbf{v}_y)$$

$$\text{s.t. } C2, C3, C5, C6, C8, C9,$$

$$C1 : z_{\min} \leq z_1 \leq z_{\max},$$

$$C11 : R_{1,n}(\mathbf{q}_1, \mathbf{P}_{\text{com},1}, \mathbf{v}_y) \geq R_{\min,1}(\mathbf{q}_1), \forall n.$$

---

**Algorithm 1** Particle Swarm Optimization Algorithm
 

---

- 1: For given  $\{\mathbf{q}_1, \mathbf{v}_y, \mathbf{P}_{\text{com},1}, \mathbf{P}_{\text{com},2}\}$ , set initial iteration number  $k = 1$ , population of  $D$  particles  $(\mathbf{p}_1^{(1)}, \dots, \mathbf{p}_D^{(1)})$  with initial random velocities  $(\mathbf{v}_{\text{PSO},1}^{(1)}, \dots, \mathbf{v}_{\text{PSO},D}^{(1)})$ , initial best local position for each particle  $(\mathbf{p}_{\text{best},1}^{(1)} = \mathbf{p}_1^{(1)}, \dots, \mathbf{p}_{\text{best},D}^{(1)} = \mathbf{p}_D^{(1)})$ , initial global best swarm position  $\mathbf{p}_{\text{best}}^{(1)} = \arg \max_{\mathbf{p}_1^{(1)}, \dots, \mathbf{p}_D^{(1)}} (\mathcal{F}(\mathbf{p}_1^{(1)}), \dots, \mathcal{F}(\mathbf{p}_D^{(1)}))$ , and initial inertial weight  $w(1) = 1$ .
  - 2: **repeat**
  - 3:   Adjust velocities  $\mathbf{v}_{\text{PSO},d}^{(k)}, \forall d$ , based on (23).
  - 4:   Update positions  $\mathbf{p}_d^{(k+1)} = \mathbf{p}_d^{(k)} + \mathbf{v}_{\text{PSO},d}^{(k)}, \forall d$
  - 5:   Update population velocities  $\mathbf{v}_{\text{PSO},d}^{(k+1)} = w(k)\mathbf{v}_{\text{PSO},d}^{(k)} + c_1\mathcal{R}_1(\mathbf{p}_{\text{best},d}^{(k)} - \mathbf{p}_d^{(k)}) + c_2\mathcal{R}_2(\mathbf{p}_{\text{best}}^{(k)} - \mathbf{p}_d^{(k)}), \forall d$
  - 6:   Update inertial weight  $w(k+1) = 1 - \frac{k}{M_1}$
  - 7:   Update local best known position  $\mathbf{p}_{\text{best},d}^{(k+1)}$  for each
  - 8:   particle and the swarm's best known position  $\mathbf{p}_{\text{best}}^{(k+1)}$  based on fitness function  $\mathcal{F}$  in (25)
  - 9:   Set iteration number  $k = k + 1$
  - 10: **until** convergence
  - 11: **return** solution  $\mathbf{q}_2 = \mathbf{p}_{\text{best}}^{(k-1)}$
- 

Sub-problem (P.1.b) is non-convex due to its objective function and constraints C5 and C11. Thus, finding the global optimal solution to sub-problem (P.1.b) is challenging. Yet, we provide the optimal solution to sub-problem (P.1.b) based on monotonic optimization theory. To this end, we start by transforming (P.1.b) into the canonical form of a monotonic optimization problem [40].

**Proposition 1.** *Sub-problem (P.1.b) is equivalent to the following monotonic optimization problem:*

$$\begin{aligned}
 (\overline{\text{P.1.b}}) : & \max_{z_1, t} C_N(\mathbf{q}_1, \mathbf{q}_2, \mathbf{v}_y) \\
 \text{s.t.} & \text{ C6,} \\
 & \overline{\text{C1a}} : z_1 - Z_{\max} \leq 0, \\
 & \overline{\text{C1b}} : z_1 - Z_{\min} \geq 0, \\
 & \overline{\text{C11a}} : a_1(z_1) + t \leq a_1(z_{\max}), \\
 & \overline{\text{C11b}} : a_2(z_1) + t \geq a_1(z_{\max}),
 \end{aligned}$$

$$\overline{\text{C11c}} : 0 \leq t \leq a_1(z_{\max}) - a_1(0),$$

where  $t \in \mathbb{R}$  is an auxiliary optimization variable,  $Z_{\min}$  is given by:

$$Z_{\min} = \begin{cases} \cos(\theta_1) \max \left\{ \frac{z_{\min}}{\cos(\theta_1)}, r_2(\mathbf{q}_2), \frac{b_{\perp}(\mathbf{q}_2)h_{\min}}{\lambda \sin(\theta_1)} \right\}, & \text{if } b_{\min} \leq b_{\perp}(\mathbf{q}_2), \\ \cos(\theta_1) \max \left\{ \frac{z_{\min}}{\cos(\theta_1)}, r_2(\mathbf{q}_2), \frac{b_{\perp}(\mathbf{q}_2)h_{\min}}{\lambda \sin(\theta_1)}, r_2(\mathbf{q}_2) \cos(\theta_1 - \theta_2(\mathbf{q}_2)) + \sqrt{b_{\min}^2 - b_{\perp}^2(\mathbf{q}_2)} \right\}, & \text{otherwise,} \end{cases} \quad (34)$$

$Z_{\max}$  is given by:

$$Z_{\max} = \begin{cases} \cos(\theta_1) \max \left\{ \frac{z_{\max}}{\cos(\theta_1)}, \frac{2\pi b_{\perp}(\mathbf{q}_2)\Delta h^{\max}}{\lambda \sin(\theta_1)\Delta\phi_{90\%}(\gamma_{\text{SNR}}^{\min}\gamma_{\text{Rg}}^{\min}\gamma_{\text{other}})} \right\}, & \text{if } b_{\min} \leq b_{\perp}(\mathbf{q}_2), \\ \cos(\theta_1) \max \left\{ \frac{z_{\max}}{\cos(\theta_1)}, r_2(\mathbf{q}_2) \cos(\theta_1 - \theta_2(\mathbf{q}_2)) - \sqrt{b_{\min}^2 - b_{\perp}^2(\mathbf{q}_2)}, \frac{2\pi b_{\perp}(\mathbf{q}_2)\Delta h^{\max}}{\lambda \sin(\theta_1)\Delta\phi_{90\%}(\gamma_{\text{SNR}}^{\min}\gamma_{\text{Rg}}^{\min}\gamma_{\text{other}})} \right\}, & \text{otherwise.} \end{cases} \quad (35)$$

Furthermore, function  $a_1$  is given by:

$$a_1(z_1) = \left( 2^{A_1 z_1 + A_2} - 1 \right) \left( z_1^2 (\tan^2(\theta_1) + 1) + (g_x - x_t)^2 + g_z^2 + 2z_1 \tan(\theta_1) [g_x - x_t]^+ \right) + \max_n \left( P_{\text{com},1}[n] \beta_{c,1} \right) + \max_{1 \leq n \leq N} \left\{ (2^{A_1 z_1 + A_2} - 1) (y[n] - g_y)^2 \right\}, \quad (36)$$

where  $A_1 = \frac{2n_B B_{\text{Rg}} \text{PRF}}{c B_{c,1}} \left( \frac{1}{\cos(\theta_1 + \frac{\Theta_{3\text{dB}}}{2})} - \frac{1}{\cos(\theta_1 - \frac{\Theta_{3\text{dB}}}{2})} \right)$ ,  $A_2 = \frac{n_B B_{\text{Rg}} \text{PRF} \tau_p}{B_{c,1}}$ , and function  $a_2$  is given by:

$$a_2(z_1) = \left( 2^{A_1 z_1 + A_2} - 1 \right) \left( 2z_1 g_z + 2z_1 \tan(\theta_1) [x_t - g_x]^+ \right) \quad (37)$$

*Proof.* Please refer to Appendix A. □

According to **Proposition 1**, sub-problem (P.1.b) can be written in the canonical form of a monotonic optimization problem given by  $(\overline{\text{P.1.b}})$ , where the feasible set is the intersection of normal set  $\mathcal{G}$ , spanned by constraints  $(\overline{\text{C1a}}, \text{C6}, \overline{\text{C11a}}, \overline{\text{C11c}})$ , and conormal set  $\mathcal{H}$ , spanned by constraints  $(\overline{\text{C1b}}, \overline{\text{C11b}})$ . The optimal solution of sub-problem  $(\overline{\text{P.1.b}})$  lies at the upper boundary of normal set  $\mathcal{G}$ , denoted by  $\partial^+ \mathcal{G}$  [40], see Figure 4a. This region is not known a priori but the sequential polyblock approximation algorithm can be used to approach this set from above. In **Algorithm 2**, we provide all steps of the proposed polyblock outer approximation algorithm that generates an  $\epsilon_1$ -approximate optimal solution to sub-problem  $(\overline{\text{P.1.b}})$ . In addition, Figure 4 depicts the operation of the polyblock algorithm. In fact, optimization variables  $z_1$  and  $t$  of sub-problem  $(\overline{\text{P.1.b}})$  are collected in vertex vector  $\mathbf{l} = (l[1], l[2])^T = (z_1, t)^T \in \mathbb{R}^2$ . Hereinafter, for ease

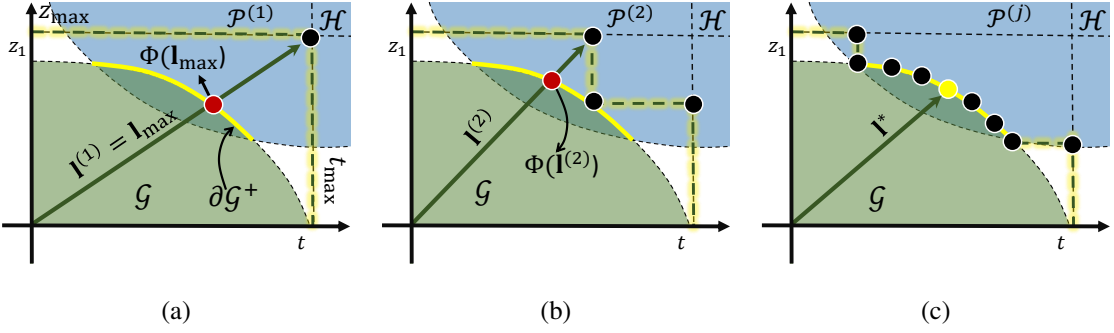


Fig. 4: Illustration of polyblock outer approximation algorithm. (a) Feasible set for a monotonic maximization problem where the normal and conormal sets are denoted by  $\mathcal{G}$  and  $\mathcal{H}$ , respectively. Vertex  $\mathbf{l}_{\max}$  is initially selected as the best vertex and its projection onto the normal set, denoted by  $\Phi(\mathbf{l}_{\max})$ , is calculated. (b) A new polyblock is constructed and the next best vertex  $\mathbf{l}^{(2)} = \arg \max_{\mathbf{l} \in \mathcal{T}^{(2)}} \{C_N(\mathbf{l}, \mathbf{q}_2, \mathbf{v}_y)\}$  is selected for projection. (c) Illustration of a tighter polyblock obtained after several iterations and the  $\epsilon_1$ -optimal solution  $\mathbf{l}^*$  is located.

---

### Algorithm 2 Polyblock Outer Approximation Algorithm

---

- 1: **Initialization:** Set polyblock  $\mathcal{P}^{(1)}$  with vertex  $\mathbf{l}^{(1)} = \mathbf{l}_{\max} = (z_{\max}, t_{\max})^T$ , vertex set  $\mathcal{T}^{(1)} = \{\mathbf{l}_{\max}\}$ , small positive number  $\epsilon_1 \geq 0$ , objective function value  $\text{CBV}^{(1)} = -\infty$ , current solution  $\mathbf{s}^{(1)} = [\cdot]$ , and iteration number  $j = 1$ .
  - 2: Remove from  $\mathcal{T}^{(1)}$  vertices  $\{\mathbf{l} \in \mathcal{T}^{(1)} | \mathbf{l} \notin \mathcal{H}\}$
  - 3: **while**  $(\mathcal{T}^{(j)} \neq \emptyset \text{ and } |C_N(\mathbf{l}^{(j)}, \mathbf{q}_2, \mathbf{v}_y) - \text{CBV}^{(j)}| > \epsilon_1)$
  - 4:     Select  $\mathbf{l}^{(j)} = \arg \max_{\mathbf{l} \in \mathcal{T}^{(j)}} \{C_N(\mathbf{l}, \mathbf{q}_2, \mathbf{v}_y)\}$
  - 5:     Compute the projection  $\Phi(\mathbf{l}^{(j)})$  onto  $\partial\mathcal{G}^+$  using **Algorithm 3**
  - 6:     **if**  $\Phi(\mathbf{l}^{(j)}) \in \mathcal{H}$  and  $C_N(\Phi(\mathbf{l}^{(j)}), \mathbf{q}_2, \mathbf{v}_y) > \text{CBV}^{(j)}$
  - 7:         **then**
  - 8:             Let the best solution  $\mathbf{s}^{(j+1)} = \Phi(\mathbf{l}^{(j)})$  and  $\text{CBV}^{(j+1)} = C_N(\Phi(\mathbf{l}^{(j)}), \mathbf{q}_2, \mathbf{v}_y)$
  - 9:         **else**
  - 10:             Set  $\mathbf{s}^{(j+1)} = \mathbf{s}^{(j)}$  and  $\text{CBV}^{(j+1)} = \text{CBV}^{(j)}$
  - 11:         **endif**
  - 12:         Set  $\mathcal{T}^{(j+1)} = \{\mathcal{T}^{(j)} \setminus \mathbf{l}^{(j)}\} \cup \left\{ \left( \Phi(\mathbf{l}^{(j)})[1], \mathbf{l}^{(j)}[2] \right)^T \right\} \cup \left\{ \left( \mathbf{l}^{(j)}[1], \Phi(\mathbf{l}^{(j)})[2] \right)^T \right\}$
  - 13:         Remove from  $\mathcal{T}^{(j+1)}$  vertices  $\{\mathbf{l} \in \mathcal{T}^{(j+1)} | \mathbf{l} \notin \mathcal{H}\}$
  - 14:         Set  $j = j + 1$
  - 15: **end while**
  - 16: **return** solution  $\mathbf{q}_1 = \left( \underbrace{x_t - s^{(j)}[1] \tan(\theta_1)}_{x_1}, \underbrace{s^{(j)}[1]}_{z_1} \right)^T$
-

---

**Algorithm 3** Bisection Search Algorithm to Compute the Upper Boundary Point
 

---

```

1: Initialization: Given  $\mathbf{I}^{(j)}$ , set  $\lambda_{\min} = 0$ ,  $\lambda_{\max} = 1$ , and error tolerance  $0 < \epsilon_2 \ll 1$ .
2: repeat
3:    $\lambda = \frac{(\lambda_{\max} + \lambda_{\min})}{2}$  ▷ Bisection middle point
4:   if  $\lambda \mathbf{I}^{(j)}$  is feasible for  $(\overline{C1a}, C6, \overline{C11a}, \overline{C11c})$  then
5:     Set  $\lambda_{\min} = \lambda$  ▷ Search in  $[\lambda, \lambda_{\max}]$ 
6:   else ▷ If  $\lambda \mathbf{I}^{(j)} \notin \mathcal{G}$ 
7:     Set  $\lambda_{\max} = \lambda$  ▷ Search in  $[\lambda_{\min}, \lambda]$ 
8:   end if
9: until  $\lambda_{\max} - \lambda_{\min} \leq \epsilon_2$  ▷ Convergence if  $\lambda_{\max} \approx \lambda_{\min}$ 
10: return  $\Phi(\mathbf{I}^{(j)}) = \lambda \mathbf{I}^{(j)}$ 

```

---

of notation,  $C_N(\mathbf{I}, \mathbf{q}_2, \mathbf{v}_y)$  refers to  $C_N((x_t - l[1] \tan(\theta_1), l[1])^T, \mathbf{q}_2, \mathbf{v}_y)$ . As shown in Figure 4a, first, we initialize a polyblock  $\mathcal{P}^{(1)}$  with corresponding vertex set  $\mathcal{T}^{(1)}$  containing vertex  $\mathbf{I}_{\max} = (z_{\max}, t_{\max})^T \in \mathbb{R}^2$ , where  $t_{\max} = a_1(z_{\max}) - a_1(0)$ . Then, in iteration  $j$ , the vertex that maximizes the objective function of sub-problem  $(\overline{P.1.b})$  is selected to create the next polyblock, i.e.,  $\mathbf{I}^{(j)} = \arg \max_{\mathbf{I} \in \mathcal{T}^{(j)}} \{C_N(\mathbf{I}, \mathbf{q}_2, \mathbf{v}_y)\}$ . The projection of vertex  $\mathbf{I}^{(j)}$  onto the normal set  $\mathcal{G}$ , denoted by  $\Phi(\mathbf{I}^{(j)})$ , is calculated and used to construct a tighter polyblock  $\mathcal{P}^{(j)}$ , see Figure 4b. The new vertex set is calculated as  $\mathcal{T}^{(j)} = \{\mathcal{T}^{(j)} \setminus \mathbf{I}^{(j)}\} \cup \left\{ \left( \Phi(\mathbf{I}^{(j)})[1], l^{(j)}[2] \right)^T \right\} \cup \left\{ \left( l^{(j)}[1], \Phi(\mathbf{I}^{(j)})[2] \right)^T \right\}$ . Once a feasible projection (i.e.,  $\Phi(\mathbf{I}^{(j)}) \in \mathcal{G} \cap \mathcal{H}$ ) that improves the objective function of sub-problem  $(\overline{P.1.b})$  is located, the corresponding vector  $\mathbf{s}^{(j+1)} = \Phi(\mathbf{I}^{(j)})$  and its objective function  $\text{CBV}^{(j+1)} = C_N(\Phi(\mathbf{I}^{(j)}), \mathbf{q}_2, \mathbf{v}_y)$  are recorded. To speed up convergence and save memory, vertices that are not in set  $\mathcal{H}$  are removed in each iteration [41]. The same procedure is repeated multiple times, such that a sequence of polyblocks converges from above to the feasible set, i.e.,  $\mathcal{P}^{(1)} \supset \mathcal{P}^{(2)} \supset \dots \supset \mathcal{P}^{(j)} \supset \mathcal{G} \cap \mathcal{H}$ , see Figure 4c. The termination criteria of the proposed algorithm are (i)  $|C_N(\mathbf{I}^{(j)}, \mathbf{q}_2, \mathbf{v}_y) - \text{CBV}^{(j)}| \leq \epsilon_1$ , for convergence, where  $\epsilon_1$  is the error tolerance, and (ii)  $\mathcal{T}^{(j)} = \emptyset$  for a non-feasible problem.

In general, **Algorithm 2** converges to an  $\epsilon_1$ -optimal solution with an exponential time complexity in the dimension of the vertex [41]. Although the polyblock outer approximation algorithm is, in general, computationally expensive, especially when the number of variables is large, for the problem at hand, the vertex dimension is only two, therefore, **Algorithm 2** obtains the optimal solution with low computational complexity. In particular, the time complexity of **Algorithm 2** stems mainly from the projection performed by **Algorithm 3**. In **Algorithm 3**, a bisection search in the interval  $[0, 1]$  is conducted with precision

$\epsilon_2$ , thus, the corresponding time complexity is  $\mathcal{O}(\log_2(1/\epsilon_2))$ . Thus, the complexity of **Algorithm 2** is  $\mathcal{O}(M_2 \log_2(1/\epsilon_2))$ , where  $M_2$  is the maximum number of iterations required for convergence.

### C. Resource Allocation Optimization

In this subsection, we aim to optimize  $\{\mathbf{v}_y, \mathbf{P}_{\text{com},1}, \mathbf{P}_{\text{com},2}\}$  given UAV formation  $\{\mathbf{q}_1, \mathbf{q}_2\}$ . Then, problem (P.1) reduces to sub-problem (P.1.c) given by:

$$(P.1.c) : \max_{\mathbf{P}_{\text{com},1}, \mathbf{P}_{\text{com},2}, \mathbf{v}_y} C_N(\mathbf{q}_1, \mathbf{q}_2, \mathbf{v}_y)$$

$$\text{s.t. C6, C10, C11, C12, C13.}$$

Sub-problem (P.1.c) is difficult to solve due to the non-convex propulsion power model used in constraint C12. Yet, we provide a low-complexity sub-optimal solution to (P.1.c) based on successive convex approximation (SCA). To start with, we introduce a slack vector  $\mathbf{u} = (u[1], \dots, u[N])^T \in \mathbb{R}^N$  and replace the propulsion power equivalently by:

$$\widetilde{P}_{\text{prop},n}(\mathbf{v}_y, \mathbf{u}) = P_0 \left( 1 + \frac{3v_y^2[n]}{U_{\text{tip}}^2} \right) + u[n] + \frac{1}{2} d_0 \rho s A v_y^3[n], \forall n. \quad (38)$$

Constraint C12 is denoted by  $\widetilde{\text{C12}}$  after replacing  $P_{\text{prop},n}$  with  $\widetilde{P}_{\text{prop},n}$  and the elements of slack vector  $\mathbf{u}$  must satisfy the following additional constraint:

$$\text{C12a} : 1 + \frac{v_y^4[n]}{4v_0^4} - \left( \frac{u^2[n]}{P_I^2} + \frac{v_y^2[n]}{2v_0^2} \right)^2 \leq 0, \forall n. \quad (39)$$

However, constraint C12a is still non-convex due to the term  $f(\mathbf{v}_y, \mathbf{u}) = \left( \frac{u^2[n]}{P_I^2} + \frac{v_y^2[n]}{2v_0^2} \right)^2$ . Therefore, in iteration  $i$  of the SCA algorithm, we approximate function  $f$  based on its Taylor series expansion around point  $\{\mathbf{v}_y^{(i)}, \mathbf{u}^{(i)}\}$  as follows:

$$\widetilde{f}(\mathbf{v}_y, \mathbf{u}) = f(\mathbf{v}_y^{(i)}, \mathbf{u}^{(i)}) + \nabla_{\mathbf{v}_y} f(\mathbf{v}_y^{(i)}, \mathbf{u}^{(i)})^T (\mathbf{v}_y - \mathbf{v}_y^{(i)}) + \nabla_{\mathbf{u}} f(\mathbf{v}_y^{(i)}, \mathbf{u}^{(i)})^T (\mathbf{u} - \mathbf{u}^{(i)}), \quad (40)$$

where  $\nabla_{\mathbf{v}_y} f(\mathbf{v}_y^{(i)}, \mathbf{u}^{(i)}) = \frac{\partial f}{\partial \mathbf{v}_y}(\mathbf{v}_y^{(i)}, \mathbf{u}^{(i)})$  and  $\nabla_{\mathbf{u}} f(\mathbf{v}_y^{(i)}, \mathbf{u}^{(i)}) = \frac{\partial f}{\partial \mathbf{u}}(\mathbf{v}_y^{(i)}, \mathbf{u}^{(i)})$ . Function  $\widetilde{f}(\mathbf{v}_y, \mathbf{u})$  is inserted in constraint C12a leading to a new convex constraint denoted by  $\widetilde{\text{C12a}}$ . The resulting convex optimization problem is given by:

$$(\widetilde{\text{P.1.c}}) : \max_{\mathbf{P}_{\text{com},1}, \mathbf{P}_{\text{com},2}, \mathbf{v}_y, \mathbf{u}} C_N(\mathbf{q}_1, \mathbf{q}_2, \mathbf{v}_y)$$

$$\text{s.t. C6, C10, C11, } \widetilde{\text{C12}}, \widetilde{\text{C12a}}, \text{C13.}$$

The proposed procedure to solve sub-problem (P.1.c) is summarized in **Algorithm 4**, where the convex approximation ( $\widetilde{\text{P.1.c}}$ ) is solved using the Python convex optimization library CVXPY [42]. It can be shown that **Algorithm 4** converges to a local optimum of sub-problem (P.1.c) in polynomial computational time complexity [43]. In particular, **Algorithm 4** involves  $3N - 1$  optimization variables and, therefore, has a

---

**Algorithm 4** Successive Convex Approximation Algorithm
 

---

- 1: For fixed  $\{\mathbf{q}_1, \mathbf{q}_2\}$ , set initial point  $\{\mathbf{v}_y^{(1)}, \mathbf{u}^{(1)}\}$ , iteration index  $i = 1$ , and error tolerance  $0 < \epsilon_3 \ll 1$ .
  - 2: **repeat**
  - 3: Determine coverage  $C_N(\mathbf{q}_1, \mathbf{q}_2, \mathbf{v}_y)$ ,  $\mathbf{u}$ ,  $\mathbf{v}_y$ ,  $\mathbf{P}_{\text{com},1}$ , and  $\mathbf{P}_{\text{com},2}$  by solving  $\widetilde{\text{(P.1.c)}}$  around point  $\{\mathbf{u}^{(i)}, \mathbf{v}_y^{(i)}\}$  using CVXPY
  - 4: Set  $i = i + 1$ ,  $\mathbf{u}^{(i)} = \mathbf{u}$ ,  $\mathbf{v}_y^{(i)} = \mathbf{v}_y$  ▷ Update solution and iteration index
  - 5: **until**  $\left| \frac{C_N(\mathbf{q}_1, \mathbf{q}_2, \mathbf{v}_y^{(i)}) - C_N(\mathbf{q}_1, \mathbf{q}_2, \mathbf{v}_y^{(i-1)})}{C_N(\mathbf{q}_1, \mathbf{q}_2, \mathbf{v}_y^{(i)})} \right| < \epsilon_3$
  - 6: **return** solution  $\{\mathbf{v}_y, \mathbf{P}_{\text{com},1}, \mathbf{P}_{\text{com},2}\}$
- 

computational time complexity of  $\mathcal{O}(M_3(3N - 1)^{3.5})$ , where  $M_3$  is the number of iterations needed for convergence [44].

#### D. Solution of Problem (P.1)

To solve problem (P.1), we use AO by solving sub-problems (P.1.a), (P.1.b), and (P.1.c), alternately, see Figure 3. To guarantee the convergence of the proposed AO **Algorithm 5**, **Algorithm 1** has to be adjusted in each iteration  $m$  to ensure a non-decreasing objective function. This can be achieved by adding one more particle to the initial PSO population of size  $D$ . The added particle represents the position of the slave UAV in the across-track plane position in the previous AO iteration, i.e.,  $\mathbf{q}_2^{(m-1)}$ , and the resulting PSO population is now of size  $D + 1$ .

In general, for non-convex optimization problems, characterized by multiple local optima, AO methods are vulnerable to getting trapped in low-quality solutions [45], which is the case for problem (P.1) due to the coupled optimization variables. In particular, the objective function is increasing w.r.t. the UAV velocity  $\mathbf{v}_y$ . However, increasing  $\mathbf{v}_y$  results in constraining the UAV formation  $\{\mathbf{q}_1, \mathbf{q}_2\}$  due to the SNR decorrelation (see constraint C6), yielding multiple local optima depending on the magnitude of the AO variable updates in each iteration. To avoid premature convergence to a low-quality solution, we propose to limit the UAV velocity update in iteration  $m$  of the AO algorithm by using a step size, denoted by  $\psi$ , as follows:

$$\mathbf{v}_y^{(m)} = \begin{cases} \mathbf{v}_y^{(m-1)} + \psi(\mathbf{v}_y - \mathbf{v}_y^{(m-1)}), & \text{if feasible for (P.1.c),} \\ \mathbf{v}_y, & \text{otherwise, } \forall m. \end{cases} \quad (41)$$

where  $\mathbf{v}_y^{(m)}$  is the UAV velocity update in the  $m^{\text{th}}$  iteration of the AO algorithm, and  $\{\mathbf{v}_y, \mathbf{P}_{\text{com},1}, \mathbf{P}_{\text{com},2}\}$  is the solution of (P.1.c) generated by **Algorithm 4**. Note that small  $\psi$  values result in smaller updates for the velocity vector, whereas  $\psi = 1$  results in the classical AO updates [45].

In **Algorithm 5**, we summarize all the steps of the solution of problem (P.1), see Figure 3. Moreover, the convergence of **Algorithm 5** is proven in **Proposition 2**.

**Proposition 2.** *Algorithm 5 is guaranteed to converge to a sub-optimal solution of problem (P.1).*

*Proof.* Please refer to Appendix B. □

---

**Algorithm 5**  $\psi$ -Step Alternating Optimization Algorithm

---

- 1: Set initial formation  $\{\mathbf{q}_1^{(1)}, \mathbf{q}_2^{(1)}\}$  and initial resources  $\{\mathbf{v}_y^{(1)}, \mathbf{P}_{\text{com},1}^{(1)}, \mathbf{P}_{\text{com},2}^{(1)}\}$ , iteration index  $m = 1$ , and error tolerance  $0 < \epsilon_4 \ll 1$ .
  - 2: **repeat**
  - 3:     Set  $m = m + 1$
  - 4:     Determine coverage  $C_N(\mathbf{q}_1^{(m-1)}, \mathbf{q}_2, \mathbf{v}_y^{(m-1)})$  and set  $\mathbf{q}_2^{(m)} = \mathbf{q}_2$  by solving (P.1.a) for fixed  $\{\mathbf{v}_y^{(m-1)}, \mathbf{P}_{\text{com},1}^{(m-1)}, \mathbf{P}_{\text{com},2}^{(m-1)}, \mathbf{q}_1^{(m-1)}\}$  using **Algorithm 1**
  - 5:     Determine coverage  $C_N(\mathbf{q}_1, \mathbf{q}_2^{(m)}, \mathbf{v}_y^{(m-1)})$  and set  $\mathbf{q}_1^{(m)} = \mathbf{q}_1$  by solving (P.1.b) for fixed  $\{\mathbf{v}_y^{(m-1)}, \mathbf{P}_{\text{com},1}^{(m-1)}, \mathbf{P}_{\text{com},2}^{(m-1)}, \mathbf{q}_2^{(m)}\}$  using **Algorithm 2**
  - 6:     Determine coverage  $C_N(\mathbf{q}_1^{(m)}, \mathbf{q}_2^{(m)}, \mathbf{v}_y)$  and  $\{\mathbf{v}_y, \mathbf{P}_{\text{com},1}, \mathbf{P}_{\text{com},2}\}$  by solving (P.1.c) for fixed formation  $\{\mathbf{q}_1^{(m)}, \mathbf{q}_2^{(m)}\}$  using **Algorithm 4**
  - 7:     **if**  $\{\mathbf{v}_y^{(m-1)} + \psi(\mathbf{v}_y - \mathbf{v}_y^{(m-1)}), \mathbf{P}_{\text{com},1}, \mathbf{P}_{\text{com},2}\}$  is feasible for (P.1.c) **then**
  - 8:         Set  $\mathbf{v}_y^{(m)} = \mathbf{v}_y^{(m-1)} + \psi(\mathbf{v}_y - \mathbf{v}_y^{(m-1)})$ ,  $\mathbf{P}_{\text{com},1}^{(m)} = \mathbf{P}_{\text{com},1}$ , and  $\mathbf{P}_{\text{com},2}^{(m)} = \mathbf{P}_{\text{com},2}$
  - 9:     **else**
  - 10:         Set  $\mathbf{v}_y^{(m)} = \mathbf{v}_y$ ,  $\mathbf{P}_{\text{com},1}^{(m)} = \mathbf{P}_{\text{com},1}$ , and  $\mathbf{P}_{\text{com},2}^{(m)} = \mathbf{P}_{\text{com},2}$
  - 11:     **until**  $\left| \frac{C_N(\mathbf{q}_1^{(m)}, \mathbf{q}_2^{(m)}, \mathbf{v}_y^{(m)}) - C_N(\mathbf{q}_1^{(m-1)}, \mathbf{q}_2^{(m-1)}, \mathbf{v}_y^{(m-1)})}{C_N(\mathbf{q}_1^{(m)}, \mathbf{q}_2^{(m)}, \mathbf{v}_y^{(m)})} \right| \leq \epsilon_4$
  - 12:     **return** solution  $\{\mathbf{q}_1^{(m)}, \mathbf{q}_2^{(m)}, \mathbf{P}_{\text{com},1}^{(m)}, \mathbf{P}_{\text{com},2}^{(m)}, \mathbf{v}_y^{(m)}\}$
- 

Leveraging the computational complexity analysis of the different sub-problems, **Algorithm 5** has  $\mathcal{O}\left(M(M_1DN + M_2\log_2(1/\epsilon_2) + M_3(3N - 1)^{3.5})\right)$  worst-case computational time complexity, where  $M$  is the number of iterations required for **Algorithm 5** to converge. **Algorithm 5** has a polynomial computational complexity, and thus, is considered to be a low-complexity algorithm. In practice, convergence is achieved in just a few iterations. Consequently, due to the low complexity of **Algorithm 5**, the  $\epsilon_5$ -optimal step size  $\psi$  can be determined by performing an exhaustive search in  $[0, 1]$  with precision  $\epsilon_5$ . Note that PSO **Algorithm 1**, being a stochastic approach, can achieve the same objective function value for sub-problem (P.1.a) for different solutions. Therefore, **Algorithm 5** might lead to slightly different results for the overall problem

TABLE II: System parameters [15], [17], [20], [26], [31].

Parameter	Value	Parameter	Value
UAV parameters		Radar parameters	
Total number of time slots, $N$	80	Reference target $x$ -coordinate, $x_t$	20 m
Maximum and minimum UAV altitudes, $z_{\max}$ and $z_{\min}$	100 and 1 m	Time slot and pulse duration, $\delta_t$ and $\tau_p$	1 and $10^{-6}$ s
Maximum and minimum UAV velocities, $v_{\max}$ and $v_{\min}$	10 and 0.1 m/s	Master look angle and radar beamwidth, $\theta_1$ and $\Theta_{3\text{dB}}$	$45^\circ$ and $30^\circ$
UAV battery capacity, $E_{\max}$	122.2 Wh	Minimum and maximum slave look angle, $\theta_{\min}$ and $\theta_{\max}$	$15^\circ$ and $75^\circ$
Minimum baseline distance, $b_{\min}$	2 m	Radar transmit and receive gains, $G_t$ and $G_r$	5 dBi
UAV weight in Newton, $W_u$	60 N	Radar transmit power and noise figure, $P_{t,1} = P_{t,2}$ and $F$	10 dBm and 7 dB
Air density, $\rho$	$1.225 \text{ kg/m}^3$	System, azimuth, and atmospheric losses, $L_{\text{sys}}$ , $L_{\text{azm}}$ , and $L_{\text{atm}}$	2, 2, and 0 dB
Fuselage drag ratio, $d_0$	0.6	Pulse repetition frequency, PRF	100 Hz
Profile drag coefficient, $\delta_u$	0.0012	Radar wavelength, $\lambda$	0.12 m
Rotor radius, $R$	0.4 m	Radar bandwidth and center frequency, $B_{\text{Rg}}$ and $f_0$	3 and 2.5 GHz
Rotor disc area, $A_e$	$0.503 \text{ m}^2$	Number of independent looks, $n_L$	4
Rotor solidity ratio, $s$	0.05	Radar system temperature, $T_{\text{sys}}$	400 K
Blade angular velocity, $\Omega$	300 rad/s	Normalized backscatter coefficient, $\sigma_0$	-10 dB
Tip speed of the rotor blade, $U_{\text{tip}}$	120 m/s	Minimum SNR and baseline decorrelation, $\gamma_{\text{SNR}}^{\min}$ and $\gamma_{\text{Rg}}^{\min}$	0.8
Incremental correction factor to induced power, $k_u$	0.1	Other decorrelation sources, $\gamma_{\text{other}}$	0.9
Communication parameters		Minimum HoA and maximum height error, $h_{\text{amb}}^{\min}$ and $\Delta_h^{\max}$	1 and 0.11 m
GS 3D location, $\mathbf{g} = (g_x, g_y, g_z)^T$	$(-100, -270, 5)^T$ m	Algorithm parameters	
Master communication bandwidth, $B_{c,1}$	1 GHz	PSO population and maximum number of iterations, $D$ and $M_1$	$2 \times 10^3$ and 1000
Slave communication bandwidth, $B_{c,2}$	1 GHz	PSO cognitive and social constants, $c_1$ and $c_2$	0.1 and 0.2
Communication reference channel gains, $\beta_{c,1} = \beta_{c,2}$	18.751 dB	PSO maximum particle velocity, $v_{\text{PSO}}^{\max}$	20 m/s
Number of bits per complex sample, $n_B$	4	Constant $O$ and number of realizations $\mathcal{N}$	500 and $10^3$
Maximum communication transmit power, $P_{\text{com}}^{\max}$	40 dBm	Error tolerance, $\epsilon_1 = \epsilon_2 = \epsilon_3 = \epsilon_4$ and $\epsilon_5$	$10^{-4}$ and $10^{-2}$

for (P.1) given the same input, which is a known property of AO algorithms when involving a stochastic algorithm [45].

## V. SIMULATION RESULTS AND DISCUSSION

In this section, we present simulation results for the proposed UAV formation and resource allocation optimization algorithm. Unless specified otherwise, the system parameters specified in Table II are employed. As explained in the previous section, since the algorithm proposed to solve (P.1) is based on stochastic optimization, different solutions may be obtained for the same input. Therefore, simulation results are averaged over  $10^3$  realizations. To assess the performance of the proposed algorithm, we consider the following benchmark schemes:

- **Benchmark scheme 1 (Classical AO):** For this scheme, we employ the classical AO algorithm [45] to solve problem (P.1), i.e., without adjusting step size  $\psi$ . This is equivalent to using **Algorithm 5** with  $\psi = 1$ .

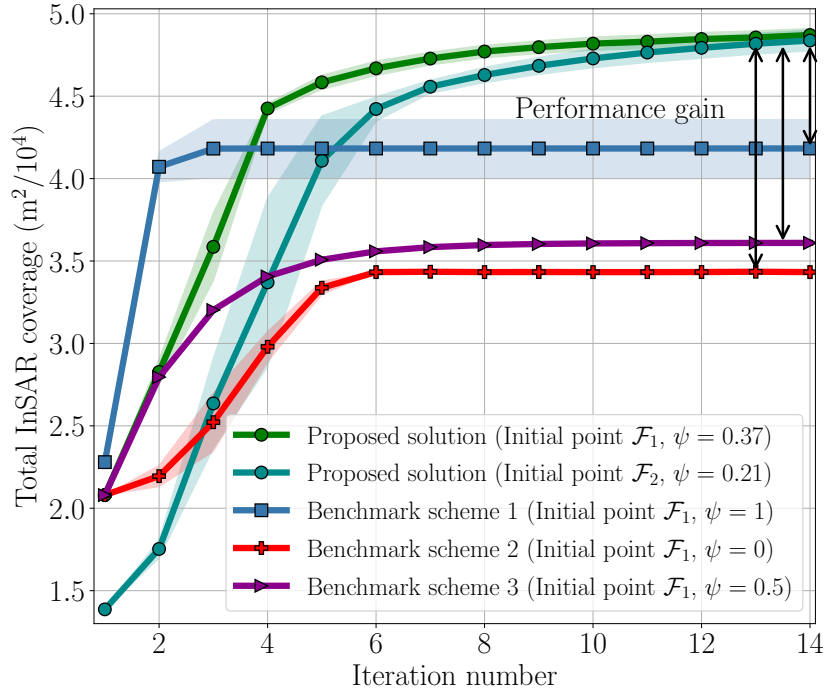


Fig. 5: Interferometric sensing coverage achieved by the proposed solution and benchmark schemes versus iteration number for different initial points, denoted by  $\mathcal{F}_1$  and  $\mathcal{F}_2$ , and given by  $\mathcal{F}_1 = \{ \mathbf{q}_1^{(1)} = (-40, 60)^T \text{ m}, \mathbf{q}_2^{(1)} = (-45, 50)^T \text{ m}, P_{\text{com},1}^{(1)}[n] = P_{\text{com},2}^{(1)}[n] = 37.78 \text{ dBm}, v_y^{(1)}[n] = 3.8 \text{ m/s}, \forall n \}$  and  $\mathcal{F}_2 = \{ \mathbf{q}_1^{(1)} = (-20, 40)^T \text{ m}, \mathbf{q}_2^{(1)} = (-45, 50)^T \text{ m}, P_{\text{com},1}^{(1)}[n] = P_{\text{com},2}^{(1)}[n] = 37.78 \text{ dBm}, v_y^{(1)}[n] = 3.8 \text{ m/s}, \forall n \}$ . Solid lines represent mean values while the shaded area corresponds to one standard deviation, i.e.,  $1\sigma$ . For the proposed algorithm, the  $\psi$  values are optimized based on an exhaustive search.

- **Benchmark scheme 2 (Fixed steady speed):** As in [1], in this scheme, we employ a fixed and steady radar platform velocity, i.e.,  $\mathbf{v}_y$  is not optimized but is set to  $\mathbf{v}_y[n] = 4 \text{ m/s}, \forall n$ . We use AO to optimize the communication powers and the UAV formation. This is equivalent to using **Algorithm 5** with  $\psi = 0$ .
- **Benchmark scheme 3 (Fixed slave look angle):** Similar to [1], we adopt a predefined look angle for the slave platform,  $\theta_2(\mathbf{q}_2) = \frac{\pi}{4}$ . Problem (P.1) is solved with a corresponding modified version of **Algorithm 5**. Here, the value of  $\psi$  leading to the best InSAR coverage is found via exhaustive search in  $[0, 1]$  with precision  $\epsilon_5$ .

In Figure 5, we investigate the convergence of the proposed AO algorithm and the different benchmark schemes by plotting the total InSAR coverage as a function of the number of iterations. The figure shows that the classical AO algorithm, i.e., benchmark scheme 1, outperforms benchmark schemes 2 and 3 due to

the joint optimization of the UAV formation and resource allocation. In fact, benchmark scheme 2 exhibits the lowest performance, underlining the importance of optimizing the instantaneous velocity of both UAVs and the slave look angle to achieve maximal sensing coverage, respectively. Furthermore, Figure 5 shows that, after convergence, the proposed solution outperforms all benchmark schemes achieving performance gains of 14.8 %, 41.21 %, and 35.74 %, compared to benchmark schemes 1, 2, and 3, respectively. In particular, the superiority of the proposed solution compared to benchmark scheme 1 is attributed to the tuning of the step size  $\psi$  to avoid premature convergence to inferior sub-optimal solutions. This performance gain comes at the cost of a lower convergence speed, as the proposed solution requires more iterations to converge. Nevertheless, overall, all benchmark schemes as well as the proposed solution converge after a relatively small number of iterations. Lastly, for different initial points  $\mathcal{F}_1$  and  $\mathcal{F}_2$ , the proposed AO-based algorithm achieves similar performance confirming resilience to the initialization.

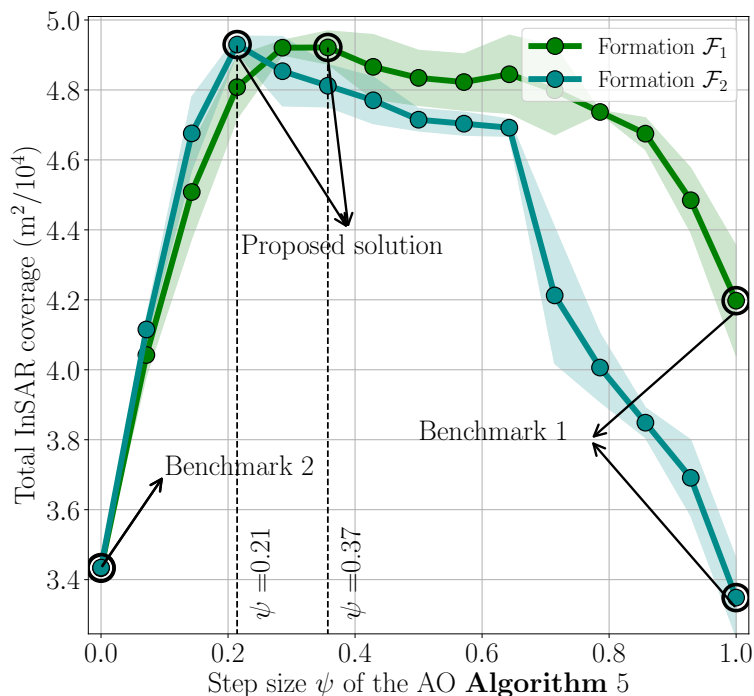


Fig. 6: Interferometric sensing coverage versus step size  $\psi$  of **Algorithm 5** for different initial points, denoted by  $\mathcal{F}_1$  and  $\mathcal{F}_2$ , see Figure 5. Solid lines represent mean values while the shaded area corresponds to one standard deviation, i.e.,  $1\sigma$ .

In Figure 6, we show the total InSAR coverage as a function of step size  $\psi$  defined in (41). The figure confirms that the performance of the conventional AO algorithm, i.e., for  $\psi = 1$ , can be significantly improved by tuning  $\psi$  in  $[0, 1]$ . Moreover, the optimal step size depends on the system parameters and the AO initialization process. For instance, the best step size for initial point  $\mathcal{F}_1$  is  $\psi = 0.37$ , while for  $\mathcal{F}_2$ , it is  $\psi = 0.21$ . Figure 6 reveals that values of  $\psi$  close to 1 and 0 are not preferable. On the one

hand, a value of  $\psi$  close to 1 results in a fast increase of the velocity in the first few iterations to improve coverage. However, this leads to low SNRs for the master and slave UAVs, i.e., a high SNR decorrelation, see (9). Therefore, the UAV formation in the across-track cannot be properly optimized and both drones have to be positioned close to the target area to keep short master and slave slant ranges that compensate for the impact of the high velocity on the SNR. On the other hand, a value of  $\psi$  close to 0 results in slow velocity updates, which allows for optimizing the UAV formation to improve coverage by opting for large master and slave slant ranges. However, the velocity can subsequently not be increased due to the SNR decorrelation constraint C6, resulting in poor performance. The proposed approach overcomes this issue by adequately selecting  $\psi$  so that the updates of the different optimization variables are well-balanced in each iteration to achieve maximum sensing coverage.

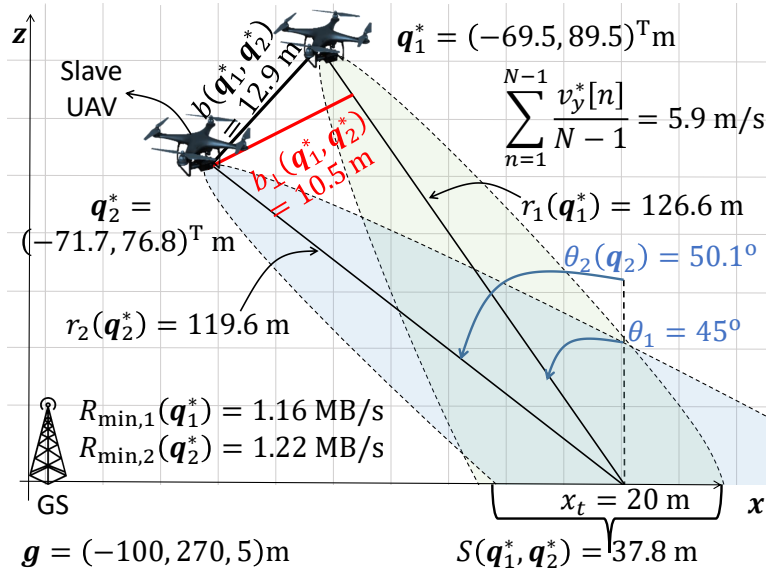


Fig. 7: Illustration of optimal UAV formation in across-track plane with key parameter values (not to scale) specified.

In Figure 7, we illustrate a UAV formation in the across-track plane obtained with **Algorithm 5**. Note that **Algorithm 5** may find different solutions leading to the same performance, therefore, the solution presented in Figure 7 is not unique. For the shown example, the perpendicular baseline is 10.5 m, leading to a relative height error of 10.5 cm and a total InSAR coverage of  $C_N = 4.95 \times 10^4 \text{ m}^2$ .

In Figure 8, we investigate the impact of the maximum communication transmit power  $P_{\text{com}}^{\text{max}}$  on the optimal UAV bistatic formation in terms of the interferometric baseline  $b$  and its perpendicular component  $b_{\perp}$ . The figure shows that the UAV formation employed for sensing is heavily affected by the communication transmit power used to offload the SAR data. In particular, for low maximum communication transmit powers, i.e.,  $P_{\text{com}}^{\text{max}} \leq 39.8 \text{ dBm}$  (blue-colored region), the proposed optimization algorithm prefers a close

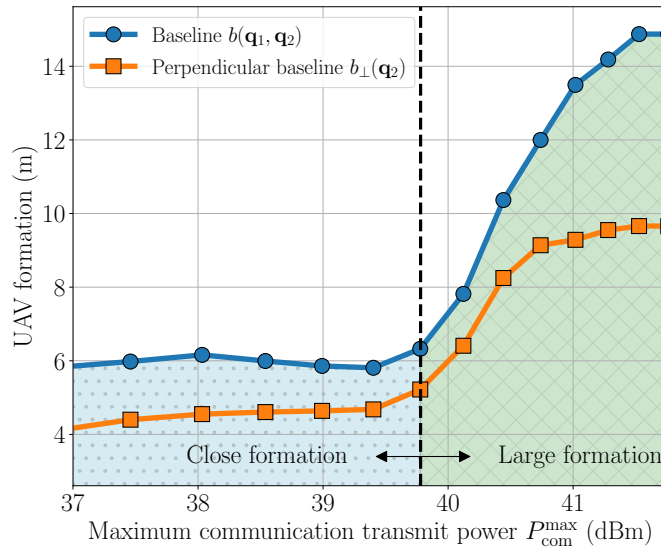


Fig. 8: Optimal UAV formation represented by the UAV baseline and perpendicular baseline versus the maximum communication transmit power for  $\beta_{c,1} = \beta_{c,2} = 19.3$  dB.

formation with short interferometric baselines as small as 6 m. In contrast, high maximum communication transmission powers, i.e.,  $P_{com}^{max} \geq 39.8$  dBm (green-colored region), result in a large UAV formation, with baselines as large as 14 m. This is because for low maximum communication transmit powers, data offloading is the performance bottleneck and, thus, **Algorithm 5** tends to position both UAVs near the target area, resulting in less sensing data. This leads to a short master slant range  $r_1$  and, therefore, a shorter perpendicular baseline is required to satisfy constraint C8, see (12). On the other hand, when the maximum communication transmit power is sufficiently high, the proposed solution optimizes the UAV formation by flying at higher altitudes for better coverage, leading to large UAV formations. This results in higher sensing data rates for the slave and master UAVs. Yet, all data from both drones can be successfully offloaded because of the high communication transmission power available.

In Figure 9, we show the optimal InSAR coverage obtained with **Algorithm 5** as a function of the minimum required SNR decorrelation for different maximum communication transmit powers. The figure reveals that the total sensing coverage decreases as the minimum required SNR decorrelation increases, i.e., as the SAR coherence requirement becomes more stringent. We distinguish between three regions in Figure 9, namely Regions I, II and III. In Region I, a high SNR decorrelation is allowed and increasing the maximum communication transmit power results in better sensing coverage due to the extended range for communications. Therefore, in Region I, the system performance bottleneck is the air-to-ground

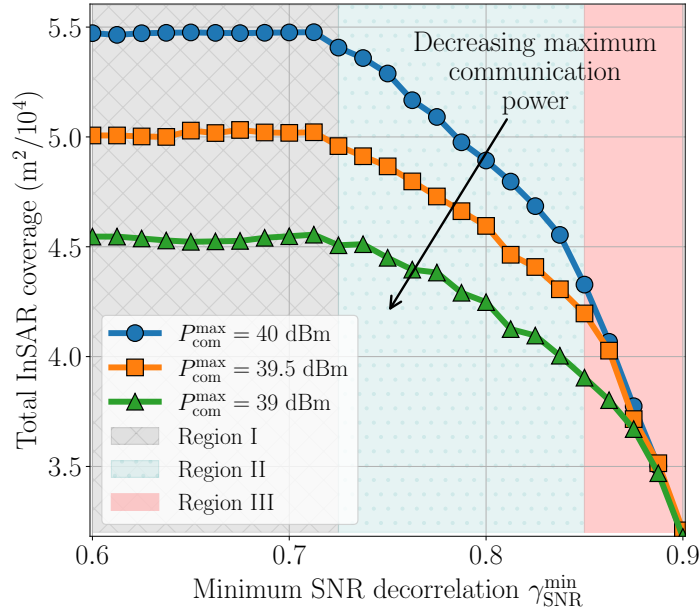


Fig. 9: Interferometric sensing coverage versus the minimum required SNR decorrelation  $\gamma_{\text{SNR}}^{\min}$  for different maximum communication transmit powers  $P_{\text{com}}^{\max}$ .

communication. In Region II, stricter sensing requirements in terms of SAR coherence are imposed and the maximum communication power has a more moderate impact on the coverage compared to Region I. Finally, in Region III, a high coherence is required and constraint C6 becomes active, i.e., sensing becomes the system performance bottleneck. Consequently, the maximum communication transmit power has little impact on the coverage performance, which highlights the interplay between communication and sensing in the considered system.

In Figure 10, we depict the average UAV velocity, given by  $\frac{1}{N-1} \sum_{n=1}^{N-1} v_y[n]$ , as function of the maximum communication transmit power for different minimum SNR decorrelation thresholds. The figure shows that the average UAV velocity increases with the maximum communication transmit power due to the increased communication range for both UAVs, which enables longer trajectories in azimuth direction. Moreover, the figure shows a strong impact of the sensing requirement on the drone speed. In fact, to achieve higher InSAR coherence, a lower speed is preferred, as it allows for improved UAV SNRs. This further confirms the need for slowly moving drones for InSAR imaging applications, especially when highly reliable sensing is demanded.

For the optimization of the considered UAV-InSAR system, we had to assume specific values for the system parameters, see Table II. In practice, the actual values of these parameters may deviate from the

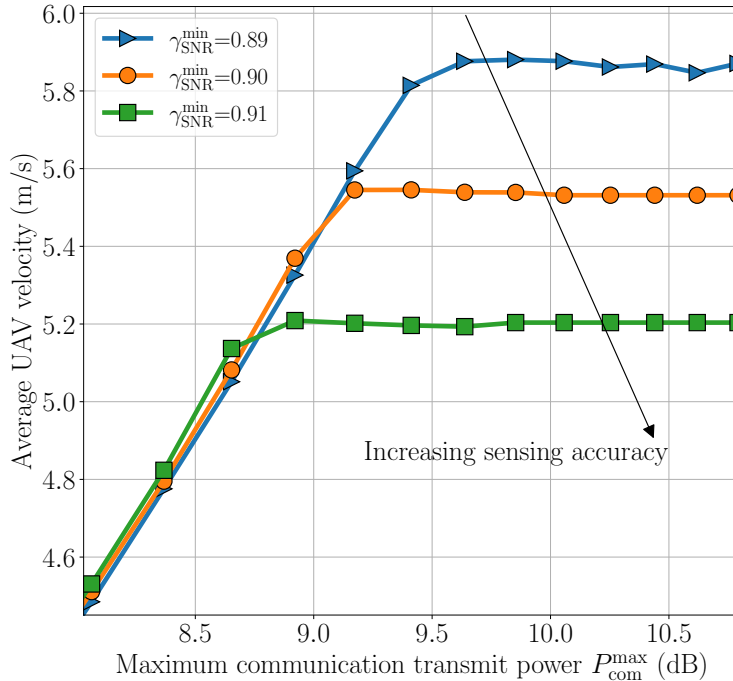


Fig. 10: Average UAV velocity as function of the maximum communication transmit power  $P_{com}^{max}$  for different values of the minimum SNR decorrelation  $\gamma_{SNR}^{min}$ .

assumed values. As a result, the solution obtained with **Algorithm 5** for the assumed values may violate the constraints of problem (P.1) for the actual parameter values. One approach to deal with this issue and make the proposed design robust to parameter uncertainties is to add safety margins to the constraints of problem (P.1). For example, the minimum SNR decorrelation,  $\gamma_{SNR}^{min}$ , may be increased by a certain percentage value,  $\Delta_E^{SNR} \times 100\%$ , such that the new minimum required SNR becomes  $(1 + \Delta_E^{SNR})\gamma_{SNR}^{min}$ . This ensures that after optimization based on the assumed parameter values, the SNR achieved for the actual parameter values does not fall below  $\gamma_{SNR}^{min}$  as long as the deviation between assumed and actual values does not become exceedingly large. The price to be paid for this increased robustness is a decrease of the achievable coverage. In Figure 11, we investigate the impact of making constraints C6, C9, and C11 more stringent to improve the robustness of the obtained solution. In particular, we increase  $\gamma_{SNR}^{min}$ ,  $R_{min,1}$ , and  $R_{min,2}$  to  $(1 + \Delta_E^{SNR})\gamma_{SNR}^{min}$ ,  $(1 + \Delta_E^{R_{min,1}})R_{min,1}$ , and  $(1 + \Delta_E^{R_{min,2}})R_{min,2}$ , respectively. Additionally, we decrease  $\Delta h^{max}$  to  $(1 - \Delta_E^h)\Delta h^{max}$ . Then, we show the InSAR coverage as a function of  $\Delta_E^{SNR}$ ,  $\Delta_E^{R_{min,1}}$ ,  $\Delta_E^{R_{min,2}}$ , and  $\Delta_E^h$ . The figure shows that introducing a margin,  $\Delta_E^h$ , that accounts for potential deviations of the maximum height error does not affect the performance. This is due to the fact that constraint C9 is inactive for the system parameters considered. However, accounting for possible 10% deviations of the minimum

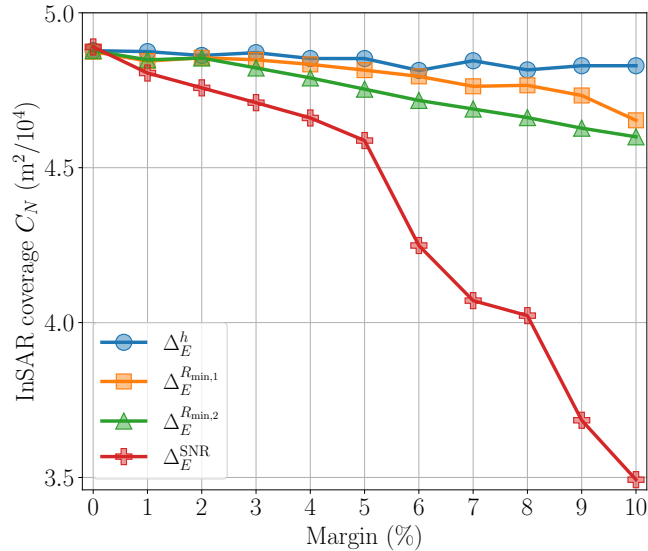


Fig. 11: Sensitivity analysis of InSAR coverage when accounting for parameter uncertainties by making the constraints of problem (P.1) more stringent.

sensing data rate for the master and slave UAVs comes with a 4.1% and 5.4% loss in total coverage, respectively. Additionally, the introduced SNR decorrelation margin,  $\Delta_E^{\text{SNR}}$ , has a more significant effect on the performance, as a loss of 27.8% in coverage is observed for a 10% deviation. This illustrates the trade-off between the robustness of the obtained solution and the achievable coverage.

## VI. CONCLUSION

In this paper, we investigated joint formation and resource allocation optimization for bistatic UAV-based 3D InSAR sensing. To assess the 3D sensing performance, the InSAR coverage, interferometric coherence, HoA, and relative height accuracy were introduced as relevant InSAR-specific performance metrics. A non-convex non-smooth optimization problem was formulated and solved for the maximization of the bistatic InSAR ground coverage while enforcing energy, communication, and sensing performance constraints. Our simulation results confirmed the superior performance of the proposed algorithm compared to several benchmark schemes and emphasized the relevance of optimizing the velocity of both radar platforms and the look angle of the slave UAV for maximum InSAR coverage. We revealed the importance of low UAV speed for high InSAR performance and showed that large areas can be mapped and offloaded to ground in real time while ground object heights can be estimated with high precision. Lastly, we highlighted the significant impact of the UAV-GS communication link on the UAV formation, and therefore, sensing performance. Potential topics for future work include the consideration of non-linear trajectories. Additionally, extending

current results to the case of more than two UAVs case is a promising research direction, for which, different communication schemes and sensing performance metrics can be used. Finally, considering a priori knowledge about the imaged scene in the optimization framework, such as the terrain type, moisture, or roughness, can also be explored.

## APPENDIX A

### PROOF OF PROPOSITION 1

Constraint C2 makes sub-problem (P.1.b) a one-dimensional optimization problem w.r.t.  $z_1$ , as it specifies a linear relation between the  $x$ - and  $z$ -coordinates of  $U_1$ . In fact, constraint C2 imposes that  $r_1(\mathbf{q}_1) = \frac{z_1}{\cos(\theta_1)}$ , and therefore, constraints C1, C3, C5, and C8 yield lower and upper bounds on  $z_1$  that are collected in variables  $Z_{\max}$  and  $Z_{\min}$ , defined in (35) and (34), respectively. In particular, for constraint C5, the lower and upper bounds on altitude  $z_1$  are derived by decomposing the baseline into its parallel and perpendicular components, i.e.,  $b(\mathbf{q}_1, \mathbf{q}_2) = \sqrt{b_{\perp}^2(\mathbf{q}_2) + b_{\parallel}^2(\mathbf{q}_1, \mathbf{q}_2)}$ , where its parallel component is given by:

$$b_{\parallel}(\mathbf{q}_1, \mathbf{q}_2) = b(\mathbf{q}_1, \mathbf{q}_2) \sin(\theta_1 - \alpha(\mathbf{q}_1, \mathbf{q}_2)). \quad (42)$$

Note that, based on constraint C2, it can be shown that the perpendicular baseline only depends on  $\mathbf{q}_2$ , see Appendix A in [1]. Hence, the baseline can be rewritten as follows:

$$b^2(\mathbf{q}_1, \mathbf{q}_2) = (r_1(\mathbf{q}_1) - r_2(\mathbf{q}_2) \cos(\theta_1 - \theta_2(\mathbf{q}_2)))^2 + b_{\perp}^2(\mathbf{q}_2). \quad (43)$$

Here, we only focus on the case where  $b_{\min} > b_{\perp}(\mathbf{q}_2)$ , as constraint C5 is always satisfied otherwise. Therefore, based on (43), the bounds on  $z_1$  are given by:

$$\frac{z_1}{\cos(\theta_1)} = r_1(\mathbf{q}_1) \geq r_2(\mathbf{q}_2) \cos(\theta_1 - \theta_2(\mathbf{q}_2)) + \sqrt{b_{\min}^2 - b_{\perp}^2}, \quad (44)$$

$$\frac{z_1}{\cos(\theta_1)} = r_1(\mathbf{q}_1) \leq r_2(\mathbf{q}_2) \cos(\theta_1 - \theta_2(\mathbf{q}_2)) - \sqrt{b_{\min}^2 - b_{\perp}^2}. \quad (45)$$

Lastly, constraint  $\overline{\text{C11}}$  is derived by expanding constraint C11 and rearranging its terms. Terms that are increasing w.r.t.  $z_1$  are assigned to function  $a_1$ , whereas terms that are decreasing w.r.t.  $z_1$  are grouped in function  $a_2$ .

## APPENDIX B

### PROOF OF PROPOSITION 2

**Algorithm 5** is an AO-based algorithm that maximizes the total InSAR coverage,  $C_N$ , and consists of four major steps. First, in sub-problem (P.1.a), the location of the slave UAV,  $\mathbf{q}_2$ , is optimized based on **Algorithm 1**. Second, in sub-problem (P.1.b), the location of the master UAV,  $\mathbf{q}_1$ , is optimized based on **Algorithm 2**. Third, in sub-problem (P.1.c), the remaining of optimization variables,  $\{\mathbf{v}_y, \mathbf{P}_{\text{com},1}, \mathbf{P}_{\text{com},2}\}$ ,

are optimized based on **Algorithm 4**. Lastly, the velocity vector is adjusted using a step size  $\psi$ , as proposed in (41). To prove the convergence of **Algorithm 5**, we show that the objective function is (i) non-decreasing in each iteration and (ii) upper-bounded [45].

First, **Algorithm 1** does not guarantee, in general, non-decreasing objective values, however, adding particle  $\mathbf{q}_2^{(m-1)}$  to the population in iteration  $m$  ensures non-decreasing InSAR coverage, as  $\mathbf{q}_2^{(m-1)}$  provides the worst-case objective value. Second, the polyblock outer approximation algorithm is also non-decreasing as the current best value, CBV, is only updated when a better solution is found. Third, the SCA **Algorithm 4** is also non-decreasing since for any generated solution,  $\mathbf{v}_y$ , the initial feasible solution,  $\mathbf{v}_y^{(m-1)}$ , represents the worst-case objective value, i.e.,  $\sum_{n=1}^{N-1} v_y^{(m-1)}[n] \leq \sum_{n=1}^{N-1} v_y[n]$ . Since the UAV formation is fixed for **Algorithm 4**, then, the coverage  $C_N$  is directly proportional to the summation of the velocities across all time slots (see (7)). Therefore, we conclude that  $C_N(\mathbf{q}_1^{(m)}, \mathbf{q}_2^{(m)}, \mathbf{v}_y^{(m-1)}) \leq C_N(\mathbf{q}_1^{(m)}, \mathbf{q}_2^{(m)}, \mathbf{v}_y), \forall m$ . Lastly, the velocity vector, adjusted using the step size  $\psi \in [0, 1]$  and denoted by  $\mathbf{v}_y^{(m)}$ , lies element-wise between  $\mathbf{v}_y^{(m-1)}$  and  $\mathbf{v}_y$ , therefore, the inequality  $\sum_{n=1}^{N-1} v_y^{(m-1)}[n] \leq \sum_{n=1}^{N-1} v_y^{(m)}[n] \leq \sum_{n=1}^{N-1} v_y[n]$  holds,  $\forall m$ . This results in  $C_N(\mathbf{q}_1^{(m)}, \mathbf{q}_2^{(m)}, \mathbf{v}_y^{(m-1)}) \leq C_N(\mathbf{q}_1^{(m)}, \mathbf{q}_2^{(m)}, \mathbf{v}_y^{(m)}), \forall m$ , and overall, a non-decreasing objective function for **Algorithm 5**.

To prove (ii), we note that the objective function, defined by the common footprint width of the platforms, is naturally upper-bounded by the individual antenna footprint widths of both master and slave UAVs. Thus, we can show that  $C_N(\mathbf{q}_1, \mathbf{q}_2, \mathbf{v}_y) \leq (S_{\text{far}}(\mathbf{q}_{\text{max}}) - S_{\text{near}}(\mathbf{q}_{\text{max}}))(N - 1)v_{\text{max}}\delta_t$ , where  $\mathbf{q}_{\text{max}} = (x_t - z_{\text{max}} \tan(\theta_1), z_{\text{max}})^T$ , which concludes the proof.

## REFERENCES

- [1] M.-A. Lahmeri *et al.*, “UAV formation optimization for communication-assisted InSAR sensing,” *proc. IEEE Int. Conf. Commun. (ICC)*, pp. 3913–3918, Jun 2024.
- [2] M. Mozaffari *et al.*, “A tutorial on UAVs for wireless networks: Applications, challenges, and open problems,” *IEEE Commun. Surv. Tutor.*, vol. 21, no. 3, pp. 2334–2360, 2019.
- [3] A. M. Haimovich, R. S. Blum, and L. J. Cimini, “MIMO radar with widely separated antennas,” *IEEE Signal Process. Mag.*, vol. 25, no. 1, pp. 116–129, 2008.
- [4] A. Moreira *et al.*, “A tutorial on synthetic aperture radar,” *IEEE Geosci. Remote Sens. Mag.*, vol. 1, no. 1, pp. 6–43, 2013.
- [5] A. Khalili *et al.*, “Efficient UAV hovering, resource allocation, and trajectory design for ISAC with limited backhaul capacity,” *IEEE Trans. Wireless Commun.*, vol. 23, no. 11, pp. 17 635–17 650, 2024.
- [6] K. Meng *et al.*, “UAV trajectory and beamforming optimization for integrated periodic sensing and communication,” *IEEE Wireless Commun. Letters*, vol. 11, no. 6, pp. 1211–1215, 2022.
- [7] Z. Lyu, G. Zhu, and J. Xu, “Joint maneuver and beamforming design for UAV-enabled integrated sensing and communication,” *IEEE Trans. Wireless Commun.*, vol. 22, no. 4, pp. 2424–2440, 2023.
- [8] N. Owens-Fahrner, S. Altrichter, and M. Cheney, “Synthetic aperture radar flight path optimization for resolution and coverage,” in *in Proc. IEEE Radar Conf.*, 2024, pp. 1–6.

- [9] Z. Sun *et al.*, “Path planning for GEO-UAV bistatic SAR using constrained adaptive multiobjective differential evolution,” *IEEE Trans. Geosci. Remote Sens.*, vol. 54, no. 11, pp. 6444–6457, 2016.
- [10] —, “Trajectory optimization for maneuvering platform bistatic SAR with geosynchronous illuminator,” *IEEE Trans. Geosci. Remote Sens.*, vol. 62, pp. 1–15, 2024.
- [11] —, “Performance analysis and system implementation for energy-efficient passive UAV radar imaging system,” *IEEE Trans. Veh. Technol.*, vol. 72, no. 8, pp. 9938–9955, 2023.
- [12] F. Xu *et al.*, “Heuristic path planning method for multistatic UAV-borne SAR imaging system,” *IEEE J. Sel. Top. Appl. Earth Obs. Remote Sens.*, vol. 14, pp. 8522–8536, 2021.
- [13] S. Hu, X. Yuan, W. Ni, and X. Wang, “Trajectory planning of cellular-connected UAV for communication-assisted radar sensing,” *IEEE Trans. Commun.*, vol. 70, no. 9, pp. 6385–6396, 2022.
- [14] M.-A. Lahmeri, W. R. Ghanem, C. Bonfert, and R. Schober, “Robust trajectory and resource optimization for communication-assisted UAV SAR sensing,” *IEEE Open J. Commun. Soc.*, vol. 5, pp. 3212–3228, 2024.
- [15] M.-A. Lahmeri *et al.*, “Trajectory and resource optimization for UAV synthetic aperture radar,” in *Proc. IEEE Global Commun. Conf.*, 2022, pp. 897–903.
- [16] H. Ren *et al.*, “Swarm UAV SAR for 3-D imaging: System analysis and sensing matrix design,” *IEEE Trans. Geosci. Remote Sens.*, vol. 60, pp. 1–16, 2022.
- [17] G. Krieger *et al.*, “TanDEM-X: A satellite formation for high-resolution SAR interferometry,” *IEEE Trans. Geosci. Remote Sens.*, vol. 45, no. 11, pp. 3317–3341, 2007.
- [18] —, “Interferometric synthetic aperture radar (SAR) missions employing formation flying,” *Proc. IEEE*, vol. 98, no. 5, pp. 816–843, 2010.
- [19] R. Bamler and P. Hartl, “Synthetic aperture radar interferometry,” *Inverse Problems*, vol. 14, no. 4, 1998.
- [20] M. Martone *et al.*, “Coherence evaluation of TanDEM-X interferometric data,” *ISPRS J. Photogramm. Remote Sens.*, vol. 73, pp. 21–29, 2012.
- [21] X. Chen *et al.*, “Performance of joint sensing-communication cooperative sensing UAV network,” *IEEE Trans. Veh. Technol.*, vol. 69, no. 12, pp. 15 545–15 556, 2020.
- [22] Z. Xiao and Y. Zeng, “Waveform design and performance analysis for full-duplex integrated sensing and communication,” *IEEE J. Sel. Areas Commun.*, vol. 40, no. 6, pp. 1823–1837, 2022.
- [23] Z. Xu *et al.*, “Effect analysis and spectral weighting optimization of sidelobe reduction on SAR image understanding,” *IEEE J. Sel. Top. Appl. Earth Obs. Remote Sens.*, vol. 12, no. 9, pp. 3434–3444, 2019.
- [24] K. Meng, X. He, Q. Wu, and D. Li, “Multi-UAV collaborative sensing and communication: Joint task allocation and power optimization,” *IEEE Trans. Wireless Commun.*, vol. 22, no. 6, pp. 4232–4246, 2023.
- [25] D. L. Schuler *et al.*, “Terrain topography measurement using multipass polarimetric synthetic aperture radar data,” *Rad. Sci.*, vol. 35, no. 3, pp. 813–832, 2000.
- [26] V. Mustieles-Perez *et al.*, “Towards UAV-based ultra-wideband multi-baseline SAR interferometry,” in *Proc. 20th European Rad. Conf.*, 2023, pp. 233–236.
- [27] M. Zink *et al.*, “The TanDEM-X mission: Overview and status,” in *Proc. IEEE Int. Geosci. Remote Sens. Symp.*, 2007, pp. 3944–3947.
- [28] I. Joughin, D. Winebrenner, and D. Percival, “Probability density functions for multilook polarimetric signatures,” *IEEE Trans. Geosci. Remote Sens.*, vol. 32, no. 3, pp. 562–574, 1994.
- [29] S. Yueh *et al.*, “K-distribution and polarimetric terrain radar clutter,” *J. Electromagn. Waves Appl.*, vol. 3, no. 8, pp. 747–768, 1989.
- [30] M. Younis, “Digital beam-forming for high resolution wide swath real and synthetic aperture radar,” Ph.D. dissertation, Karlsruhe, Univ., 2004.

- [31] Y. Zeng, J. Xu, and R. Zhang, "Energy minimization for wireless communication with rotary-wing UAV," *IEEE Trans. Wireless Commun.*, vol. 18, no. 4, pp. 2329–2345, 2019.
- [32] J. Schneider and S. Kirkpatrick, *Stochastic Optimization*. Springer Science & Business Media, 2007.
- [33] D. Wang, D. Tan, and L. Liu, "Particle swarm optimization algorithm: an overview," *Soft Computing*, vol. 22, pp. 387–408, 2018.
- [34] J. Kennedy and R. Eberhart, "Particle swarm optimization," in *Proc. Int. Conf. Neural Netw.*, vol. 4, 1995, pp. 1942–1948.
- [35] K. E. Parsopoulos *et al.*, "Particle swarm optimization method for constrained optimization problems," *Intelligent Technologies: Theory and Application: New Trends in Intelligent Technologies*, vol. 76, no. 1, pp. 214–220, 2002.
- [36] T. M. Shami *et al.*, "Particle swarm optimization: A comprehensive survey," *IEEE Access*, vol. 10, pp. 10 031–10 061, 2022.
- [37] J. Robinson and Y. Rahmat-Samii, "Particle swarm optimization in electromagnetics," *IEEE Trans. Antennas Propag.*, vol. 52, no. 2, pp. 397–407, 2004.
- [38] Q. He and L. Wang, "An effective co-evolutionary particle swarm optimization for constrained engineering design problems," *Eng. Appl. Artif. Intell.*, vol. 20, no. 1, pp. 89–99, 2007.
- [39] H. Garg, "A hybrid PSO-GA algorithm for constrained optimization problems," *Appl. Math. Comput.*, vol. 274, pp. 292–305, 2016.
- [40] Y. J. A. Zhang *et al.*, "Monotonic optimization in communication and networking systems," *Found. Trends Netw.*, vol. 7, no. 1, pp. 1–75, Oct. 2013.
- [41] H. Tuy, "Monotonic optimization: Problems and solution approaches," *SIAM J. Optim.*, vol. 11, no. 2, pp. 464–494, Nov. 2000.
- [42] S. Diamond and S. Boyd, "CVXPY: A python-embedded modeling language for convex optimization," *J. Mach. Learn. Res.*, vol. 17, no. 83, pp. 1–5, 2016.
- [43] Q. T. Dinh and M. Diehl, "Local convergence of sequential convex programming for nonconvex optimization," *Recent Adv. Optim. Appl. Eng.*, pp. 93–102, 2010.
- [44] G. Zhang, Q. Wu, M. Cui, and R. Zhang, "Securing UAV communications via joint trajectory and power control," *IEEE Trans. Wireless Commun.*, vol. 18, no. 2, pp. 1376–1389, 2019.
- [45] J. C. Bezdek and R. J. Hathaway, "Some notes on alternating optimization," in *Proc. AFSS Int. Conf. Fuzzy Sys.* Springer, 2002, pp. 288–300.